CHALMERS
UNIVERSITY OF TECHNOLOGY

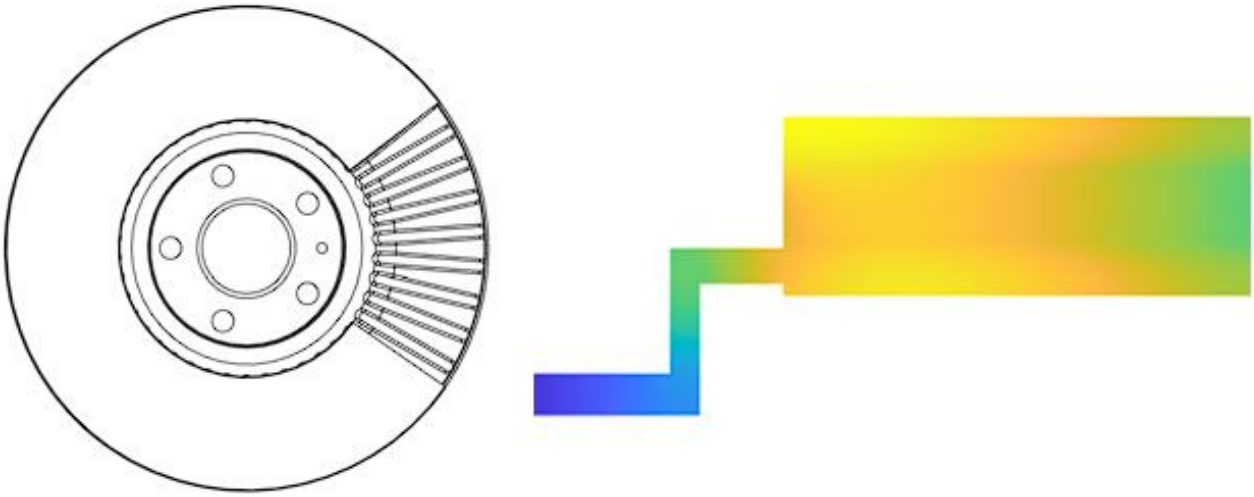

A scaled axisymmetric finite element model for heat flow in ventilated brake rotors

Master's thesis in Mobility Engineering

Elias Håland
Erik Sparf

DEPARTMENT OF INDUSTRIAL AND MATERIALS SCIENCE

CHALMERS UNIVERSITY OF TECHNOLOGY
Gothenburg, Sweden 2025
www.chalmers.

Master's thesis 2025

A scaled axisymmetric finite element model for heat flow in ventilated brake rotors

Elias Håland, Erik Sparf

CHALMERS
UNIVERSITY OF TECHNOLOGY

Department of Industrial and Materials Science
Chalmers University of Technology
Gothenburg, Sweden 2025

A scaled axisymmetric finite element model for heat flow in ventilated brake rotors
Elias Håland
Erik Sparf

Supervisor: Dimosthenis Floros, Volvo Car Corporation, Brake system CAE
Examiner and supervisor: Fredrik Larsson, Industrial and Materials Science

Master's Thesis 2025
Department of Industrial and Materials Science
Chalmers University of Technology
SE-412 96 Gothenburg
Sweden
Telephone +46 31 772 1000

Typeset in Microsoft Word
Gothenburg, Sweden 2025

A scaled axisymmetric finite element model for heat flow in ventilated brake rotors
Elias Håland
Erik Sparf
Department of Industrial and Materials Science
Chalmers University of Technology

Abstract

The aim of this thesis was to develop a finite element model of the heat flow in a ventilated disc brake that is both accurate and computationally efficient. The model is intended to be used during the early stages of development for brake components. It must capture the out-of-plane effects on the non-axisymmetric ventilation layer while remaining two dimensional to allow for fast simulations. To accomplish this an enriched two-dimensional model was developed where each edge and face are scaled based on their size in the out of plane direction. The scaling factor was acquired by doing a geometry mapping of each surface and volume on a three-dimensional model of the brake disc, using it to integrate the weak-form over the out of plane dimension. The scaled axisymmetric model was validated against the result of a high-fidelity three-dimensional model of the brake disc supplied by Volvo Car Corporation.

The difference between the simulation result of the scaled two-dimensional axisymmetric model and the three-dimensional model was only about 1% when considering heating of an insulated wheel. When adding boundary condition pertinent to the convection over all surfaces, the difference in simulation results becomes about 5%. In both simulation cases, the scaled two-dimensional axisymmetric model accurately captures the average temperature distribution of the three-dimensional model.

This accuracy is good considering the difference in computational cost between the models. The scaled two-dimensional model takes minutes to compute while the three-dimensional model takes several hours, which is a good trade off during the early development stages of a brake rotor.

Keywords: ventilated brake rotor, ventilated brake disc, finite element modeling, FE, 2D simulation, axisymmetric modeling, straight radial vanes

Preface

This report presents the outcome of our master's thesis project carried out at the Department of Industrial and Material Science at Chalmers University of Technology during the spring of 2025.

Acknowledgement

Firstly, we would like to sincerely thank our supervisor Dimosthenis Floros for his continuous support and guidance throughout this thesis. We greatly appreciate the knowledge and feedback you have shared with us. Secondly, we would also like to extend our gratitude to our examiner and supervisor Fredrik Larsson for his guidance and insights during our advisory meetings.

Elias Håland, Erik Sparf, Gothenburg, June/2025

List of Acronyms

Below is a list of acronyms used throughout this thesis, presented in alphabetical order:

FE	Finite Element
HTC	Heat Transfer Coefficient
VCC	Volvo Car Corporation
1D	One-Dimensional
2D	Two-Dimensional
3D	Three-Dimensional

Contents

List of figures

1. Introduction

1.1 Background

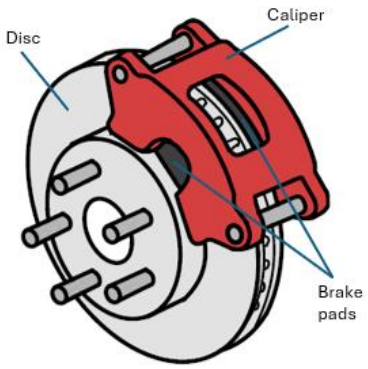

Figure 1: Typical brake system assembly. Adapted from (Bhandari & Mane, 2020)

The automative brake system is designed to convert the kinetic energy of a moving vehicle into thermal energy through friction, slowing the vehicle down. A typical assembly of a disc brake system is shown in Figure 1, which comprises of a brake disc, -pads and -caliper. During a brake application, hydraulic fluid pressure is generated in the tandem master cylinder of the brake actuation unit, which is then transmitted to the pistons in the caliper, exerting a normal force to the brake pad. This causes contact between the brake disc and pad, generating friction at the disc-pad interface, producing brake torque around the wheel axle reducing its rotational velocity. As a result, the vehicle decelerates due to the corresponding brake force that develops due to slip at the tire-road contact patch.

During long and repetitive brake applications, the brake rotor is subjected to high thermal loads caused by the frictional contact at the disc-pad interface, generating heat. The temperature in the rotor disc-pad interface is of interest during design due to the temperature dependence of friction and material properties. Elevated temperatures can cause brake fade and induce thermal stresses, in addition to mechanical frictional stresses. Furthermore, increased temperature may cause out-of-plane deformations in the rotor, affecting the contact pressure between brake pad and disc, compromising braking.

Volvo Car Corporation (VCC) is currently using Finite Element (FE) simulations to predict the temperature distribution in brake rotors during the conceptual design phase of the next generation vehicle projects. More specifically, simulations featuring an in-house 2D axisymmetric model provide insight into the thermal behavior of brake rotors already at early stages of development, where rapid design iterations with sufficient accuracy are essential. To effectively dissipate significant frictional heat generated during braking, ventilated disc brakes are common, as in the case with VCC. However, the geometry of the ventilated discs, along with the locally applied frictional heat input at the disc-pad interface, induce a temperature distribution that varies both circumferentially and through the disc thickness. Ideally, a 3D model would be needed to accurately resolve the effects of the 3D temperature distribution, which are not fully captured by the existing 2D axisymmetric FE-model. However, a 3D model significantly increases computation runtime.

Therefore, to achieve both accuracy and computational efficiency, the in-house FE-model must incorporate these effects without resorting to a full 3D model.

1.2 Aim

The aim of the thesis is to develop a FE model of the heat flow in a ventilated disc brake that is both accurate and computationally efficient. The model must capture out-of-plane effects on temperature distribution and improve capturing ventilation effects matching the accuracy of a 3D model, while maintaining the computational efficiency of a 2D axisymmetric model. To achieve this, the standard axisymmetric heat flow formulations will be enriched to account for convection through the ventilation layer. The realization of the aim is structured around the following objectives:

- Perform a literature study of current approaches for thermal bake modeling
- Develop a method to capture the out-of-plane effects on the brake rotor
- Validate the model against a 3D model supplied by VCC with respect to result accuracy and benchmarked runtime speed

1.3 Scope and limitations

The project builds on the existing 2D axisymmetric model developed by VCC, by extending it to better account for brake cooling of ventilated brake discs. The new model targets straight radial vane geometries and uses inputs such as the number of vents, the angle one vent occupies, and ventilation layer thickness. The disc geometry is formulated in a polar coordinate system, resulting in “pie shaped” vents and vanes, which differ from the actual vanes with continuous width. Additionally, the model does not capture geometric features such as corner radius, chamfers, or non-repetitive pattern features.

Frictional heat input to the disc is simplified as a uniformly distributed heat flux, with heat partitioned between the disc and pads. Temperature dependent material properties and heat transfer coefficient due to radiation are linearized. Convective heat transfer coefficient varies between boundary condition edges, capturing local heat removal rate as a function of the rotational velocity of wheel. For simplicity, edges with similar values are grouped.

1.4 Specification of the issue being investigated

- Develop a thermal model that captures ventilation thickness and out-of-plane effects comparable to a 3D model, while maintaining computational expense comparable to a 2D axisymmetric model.
- What model fidelity is required for different analysis scopes
- How boundary conditions should be modeled in simpler models for valid comparison against 3D reference problems
- How far the enriched 2D model can cope compared to their 3D reference

2. Heat flow in brake rotor

2.1 Heat flow of ventilation brake rotor

During braking, friction between the brake pad and disc converts the vehicle's kinetic energy into heat, raising the temperature of the rotor. This heat spreads from the contact surface through the disc material by conduction, making the rotor store thermal energy. The stored heat in the rotor dissipates via the conduction, radiation and convection phenomena, as illustrated in Figure 2.

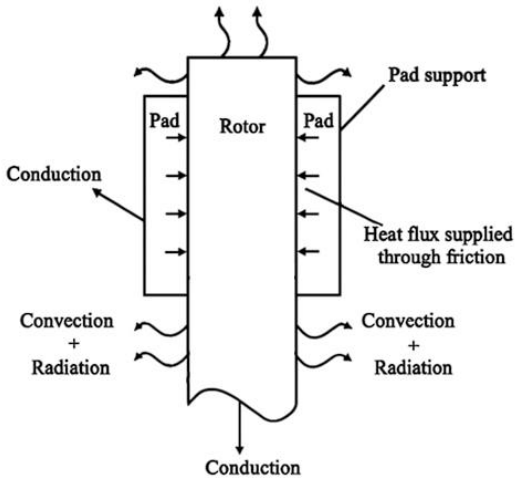

Figure 2: Heat flow of a friction brake rotor. Adapted from (F. Talati & S. Jalalifar, 2008)

The heat dissipation will occur through conduction into the brake pad and hub continuing to wheel assembly, radiation to surrounding components, and convection to the air. Managing rotor temperatures relies on maximizing these three heat transfer mechanisms. Conduction effectively transfers heat from the friction surface to colder regions, but this typically requires an increase of mass to provide sufficient thermal capacity. Heat dissipation through radiation has its greatest effects at high temperatures but is generally small during normal braking temperatures. Convection to the atmosphere is typically the largest contribution and primary means of heat dissipation of the brake rotor, and can be described by Newton's law of cooling:

$$Q = h_c A(T - T_\infty) \tag{1}$$

where, Q is the rate of heat transfer, h_c the convective heat transfer coefficient, A the rotor surface area, T the rotor surface temperature and T_∞ the ambient air temperature. From this expression, it is evident that to maximize heat transfer from the rotor requires an increase in either the heat transfer coefficient h_c or the surface area A. The amount of surface area possible to increase is confined by space available and by the requirement to minimize unsprung mass. Therefore, improvement in cooling is best achieved by increasing the heat transfer coefficient (HTC). For this reason, internally ventilated rotors are common, as both surface area and the HTC, due to forced convection, are increased. Additionally, it has a low impact on unsprung mass and rotational inertia.

The forced convection in internally ventilated rotors is generated by airflow through internal vents, which function as a centrifugal fan, illustrated in Figure 3. As the brake rotor spins, air is drawn into the center by localized low pressure and ejected outward through the vents by centrifugal force, increasing the mass flow rate and thereby enhancing the convection HTC in the vents.

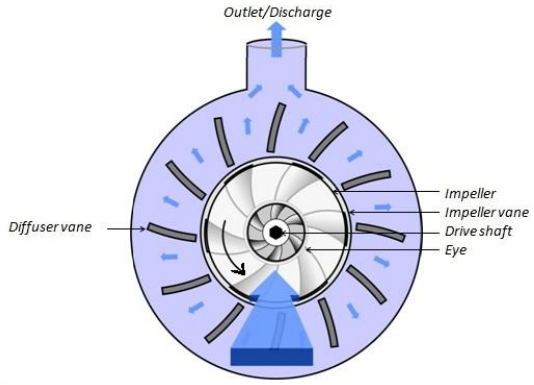

Figure 3: Airflow of a centrifugal fan. Reproduced from ("Centrifugal Pumps," *2025)*

However, airflow interacting with a ventilated brake rotor is more complex than the centrifugal fan analogy suggests, and precise estimation of the convective HTC is required to accurately predict brake temperature. Accurate determination of this coefficient is considered challenging due to its spatial and temporal variability (Vdovin & Le Gigan, 2020; Zhang et al., 2024). This variability arises from changes in vehicle velocity, surrounding aerodynamics, and localized airflow shaped by the brake rotor's geometry. Airflow's nonlinear and turbulent characteristics contribute to its sensitivity, making accurate quantification of the convective HTC particularly challenging, as even minor deviations in geometry or aerodynamics can significantly affect the cooling effect.

2.2 Heat transfer modeling

Accurate modeling of heat transfer coefficients is critical for predicting the temperature of the brake rotor and obtaining reliable simulation results. For early brake design, the thermal simulation model must strike a balance between accuracy and simplicity, that is, to represent real world heat transfer behavior while remaining computationally efficient. This chapter examines common expressions and assumptions in the modeling of HTC, with emphasis on modeling with sufficient precision and without introducing excessive complexity or increase in simulation runtime.

2.2.1 Convection

The difficulty in accurately determining convection HTC, as highlighted in Chapter 2.1, poses a challenge in early brake rotor design and thermal modeling, where changes in geometry and aerodynamics alter the heat transfer rate, requiring the simulation tool to remain accurate throughout these changes. Thus, the HTC model must sufficiently capture these variations.

The convective HTC can be determined using numerical, experimental and analytical methods. The numerical approach typically involves Computational Fluid Dynamics simulations coupled with heat transfer analysis. Experimental methods rely on direct measurements of temperature, heat flux, and air flow. Both methods are often performed over a range of vehicle speeds to generate HTC characteristics. Analytical methods employ empirical correlations, such as Nusselt number, a dimensionless parameter derived from idealized geometries and flow conditions [(Sheridan et al., 1988)] or alternatively modeled as a function of vehicle speed. Analytical methods are often calibrated against numerical or experimental data to improve accuracy. While numerical and experimental methods offer greater accuracy, analytical methods provide a computational efficient approach to estimate HTC, making it suitable for early-stage design.

2.2.2 Radiation

The radiative HTC comes from the Steffan Boltzmann's law:

$$h_r(T) = \varepsilon_e \sigma [T^4 - T_\infty^4] \tag{2}$$

where ε_e is the emissivity, σ the Steffan Boltzmann constant, T the surface temperature and T_∞ the ambient temperature. (Kingston, 1995)

Radiation is inherently nonlinear due to the fourth power temperature dependence, making it significantly more computationally expensive. Linearization of the equation is a potential way of making it less computationally expensive, but with the consequence of losses in accuracy.

2.2.3 Friction heat

The majority of the heat generated at the disc-pad interface during braking is absorbed by the disc and the rest by the pad, based on their thermal properties and contact characteristics. Two thermal contact models are commonly used (Dufré, 2005). Perfect contact assumes equal surface temperature between disc and pad, while imperfect contact considers the heat resistance between disc and pad caused by a third body of detached particles commonly known as brake dust that forms during braking. Newcomb demonstrates that pad heat absorption can generally be negligible except during prolonged braking events, when it absorbs 10 to 20 percent of the heat (Newcomb, 1960).

Heat flux depends on the friction coefficient, relative sliding velocity, contact geometry between disc and pad and the pressure distribution. Since the friction coefficient decreases with temperature due to brake fade at elevated temperatures, modeling it accurately is challenging and often simplified. Pressure distribution can typically be idealized as either uniform pressure or uniform wear, with the former being valid for new pads and the latter for worn pads (F. Talati & S. Jalalifar, 2008).

2.2 The existing axisymmetric simulation tool

As part of this thesis, the work builds upon an existing MATLAB simulation tool developed by VCC in-house, necessitating an understanding of the existing tool, which will be outlined in this section. This tool is a 2D axisymmetric thermal simulation model of the brake disc, designed to support the early-stage conceptual design of brake discs. By entering heat input, disc geometry dimensions and material properties, the model computes the temperature distribution through the disc thickness, along with the point temperature at the disc-pad interface. This provides engineers insight into the effects of geometry changes and material selection, with the added advantage of rapid iterations due to the lower computational runtime of the 2D model compared to 3D modeling.

2.2.1 AMS brake test

The AMS brake test is a non-standardized, yet widely recognized brake testing procedure developed by the German automotive magazine *Auto motor und Sport* (*Brake-Tests Imc Test & Measurement GmbH*, n.d.). It is used to evaluate the performance of friction brakes under thermally intensive conditions. The test involves a series of consecutive high-speed braking events that generate significant thermal loads, making it suitable for assessing brake fade and informing brake disc design. Brake fade is a phenomenon in which increased temperatures reduce the coefficient of friction between the disc and pad, leading to longer braking distances that design efforts aim to reduce.

In this thesis, the AMS test is defined as 11 consecutive ABS-controlled, full-stop braking events

from a high velocity. The normalized velocity profile from testing is shown in Figure 4.

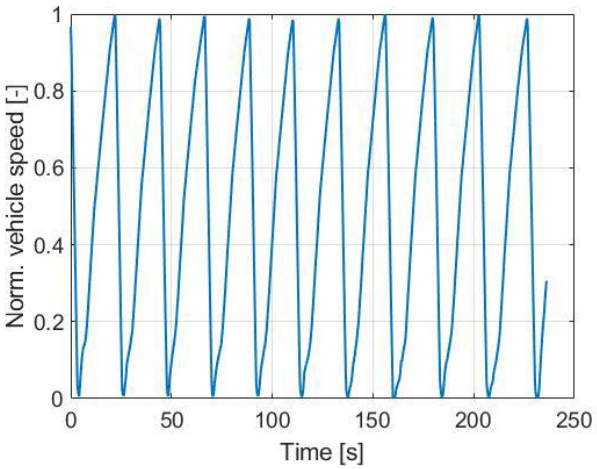

Figure 4: Normalized vehicle speed profile for an AMS test

2.2.2 Computational Domain

The axial symmetry of the brake disc shown in Figure 5 can be represented by a two-dimensional axisymmetric model based on a cross-sectional view obtained from a through thickness cut of the disc. To further simplify the model, the 2D geometry of the disc section view is idealized as the computational domain of Figure 6. In this figure, E represents edges and F represents faces, color-coded in black and red, respectively.

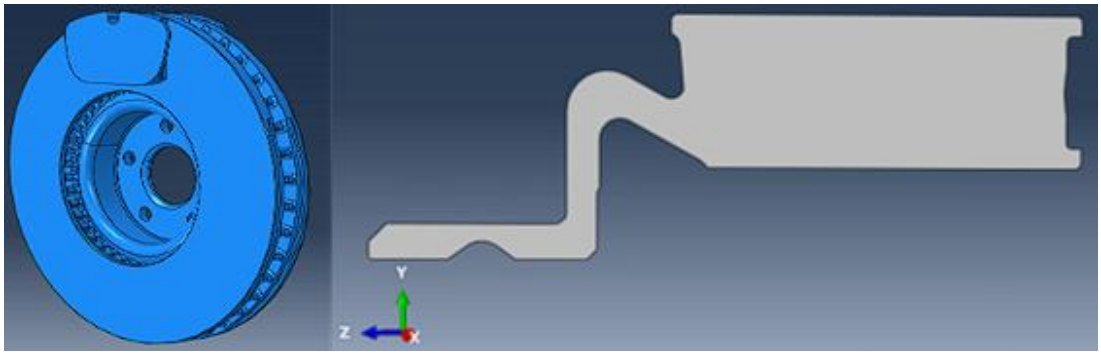

Figure 5: Ventilated brake disc with pad, and corresponding 2D axisymmetric view of the disc

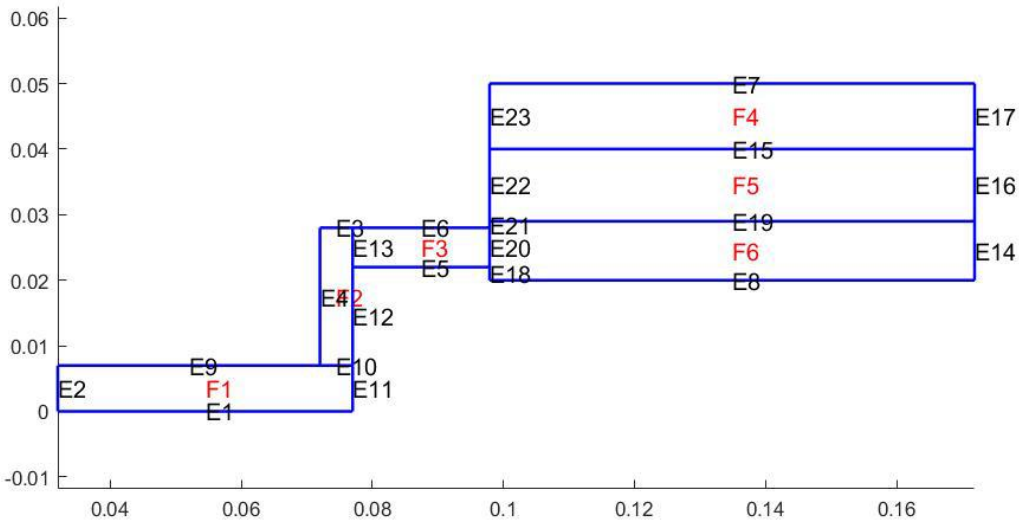

Figure 6: Idealized geometry and computational domain

2.2.3 Thermal material properties

The brake discs are made from grey cast iron. Laboratory testing found that its thermal properties, such as thermal conductivity and specific heat capacity, exhibit a near-linear variation with respect to temperature. Figure 7 presents fitted lines used in the thermal modeling of the brake rotors, displayed in a normalized form.

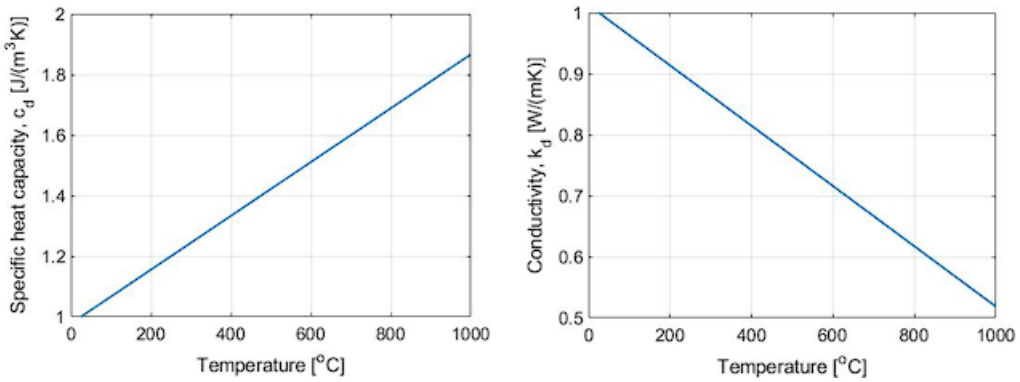

Figure 7: Normalized thermal properties of cast iron

A temperature dependence of the thermal properties results in a non-linear problem. To keep it linear and reduce its computational runtime, the assumption is made that the thermal properties depend on the temperature at the previous time step, T*. Small time steps are chosen to limit the approximation error introduced from this approach, with only minor differences observed to the non-linear solution.

2.2.4 Ventilation

The ventilated portion of the disc, represented by face F5 in Figure 6, is modeled as an effective solid disc layer with custom material properties. These properties account for the combined effect of vents and the solid structure separating them, and are calibrated to align with temperature testing data from the actual disc. The calibration factors $\varepsilon_k, \varepsilon_c$ and ε_ρ scale the conductivity, specific heat capacity and density respectively of the disc material properties. The implementation of material properties to each face of the computational domain are determined by

$$k_d(T^*, \boldsymbol{x}) = \varepsilon_k(\boldsymbol{x}) \left[k_{d0} + \frac{k_{d0}[32 - k_{d0}]}{k_\alpha[700 - 25]} [T^*(\boldsymbol{x}) - 25] \right] \tag{3}$$

$$c_d(T^*, \boldsymbol{x}) = \varepsilon_c(\boldsymbol{x}) \left[c_{d0} + \frac{c_{d0}[800 - c_{d0}]}{c_\alpha[700 - 25]} [T^*(\boldsymbol{x}) - 25] \right] \tag{4}$$

$$\rho_d(x) = \varepsilon_\rho(x) \rho_{d0} \tag{5}$$

where T^* is the temperature in the previous time step, k_{d0}, c_{d0} and ρ_{d0} are the properties of the disc material at 25 degrees Celsius and, k_α and c_α are material parameters not disclosed here due to VCC intellectual property protection restrictions. Scaling factors for the effective thermal properties in the ventilation layer are calibrated within the range of 0 to 1. For all other faces, the scaling factors are set to 1.

2.2.5 Friction heat

The total amount of heat generated per wheel due to contact at the brake disc-pad interface during braking is modeled dependent on several parameters. These include the disc-pad friction coefficient μ, the pressure exerted by the brake caliper piston p, the piston area A_c, the effective radius of the caliper R_e, the vehicle's longitudinal velocity $v(t)$, and the dynamic rolling radius of the tire R_{tir}. The heat generated can be expressed as a time-dependent function of these variables:

$$h_{tot}(t) = 2\mu(t)p(t)A_cR_e\frac{v(t)}{R_{tir}} \tag{6}$$

To determine the heat flux per disc surface, the total heat input is partitioned between the disc and pad derived from their geometric and material properties, using Charron's formula (Charron & Vernotte Pierre, 1939). The resulting heat outflux, denoted as $\hat{h}$, is assigned as a natural boundary condition on edges E7 and E8 in the idealized geometry, Figure 6.

2.2.6 Convection

Heat transfer due to convection is modeled along all edges of the domain. The coefficient varies between different edges, reflecting difference in heat removal rates caused by local conditions. These variations are primarily driven by the rotation of the wheels, which induces varying degrees of forced convection over the surface. To capture this behavior, the convective HTC is modeled to vary as a second-degree polynomial function of the longitudinal velocity of the wheels:

$$h_c(x,t) = \alpha_0(x) + \alpha_1(x)v_w(t) + \alpha_2(x){v_w}^2(t) \tag{7}$$

This expression is then reformulated in terms of the rotational velocity of the wheel ω , with the HTC at each boundary point expressed as a function of its radial coordinate r:

$$h_c(x,t) = \alpha_0(x) + \alpha_1(x)\omega(t)r + \alpha_2[\omega(t)r]^2 \tag{8}$$

A velocity dependent convection coefficient was considered only on the friction ring, the portion of the rotor adjacent to the frictional contact, where the temperature rise in the rotor relative to the ambient temperature is most significant. To limit the number of calibration parameters, on boundaries not in the friction ring α_1, α_2 is set to zero. For the same reason, edges of the domain that share similar values of α_0, α_1 and α_2 are grouped together.

2.2.7 Radiation

Heat transfer due to radiation is modeled along all edges of the domain. The current HTC model employs Steffan Boltzmann's law, as detailed in equation 2.

2.2.8 Calibration tool

The calibration tool iteratively refines calibration parameters to achieve close agreement between simulation results and experimental temperature measured from the AMS brake disc test.

During the AMS test, the temperature at the disc-pad interface rises significantly causing brake fade, a phenomenon in which the coefficient of friction reduces due to the temperature increase. To capture this effect in the model, the friction coefficient μ is allowed to vary discretely from one braking cycle to the next in the AMS test. Each discrete value μ is a calibration parameter. A summary of all calibrated parameters is provided in Table 1.

Table 1: Model parameters for calibration

Parameter	Unit	Location
α_0	$[\mathrm{W/(m^2\,K)}]$	E_n
$\{\alpha_0, \alpha_1, \alpha_2\}$	$\{[\mathrm{W/(m^2\,K)}], [\mathrm{W/(m\,s\,K)}], [\mathrm{W/(s^2\,K)}]\}$	E_f
$\{\alpha_0, \alpha_1, \alpha_2\}$	$\{[\mathrm{W/(m^2\,K)}], [\mathrm{W/(m\,s\,K)}], [\mathrm{W/(s^2\,K)}]\}$	E_v
ε_k	$[-]$	$F5$
ε_c	$[-]$	$F5$
ε_ρ	$[-]$	$F5$
ε_e	$[-]$	Γ_r
$\mu_i,\ i = 1, 2, \cdots, 10$	$[-]$	E_p

2.3 Ventilation design

Brake disc ventilation designs vary but can generally be grouped into two main types: vanes and pins, as shown in Figure 8 on the left and right, respectively.

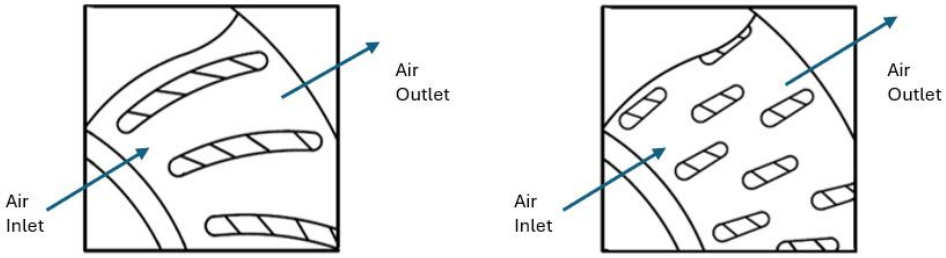

Figure 8: Ventilation types with vanes and pins, respectively. Adapted from (G. et al., 2002)

Vane type is the most common in the automotive industry and adopted by VCC, featuring straight radial vanes rather than the curved vanes shown in the figure. The straight radial vane forms the primary modeling objective, with a focus on capturing its surface area and forced convection contribution.

2.4 Established 2D ventilation model approach

To meet the aim of the thesis, the 2D model must capture out-of-plane temperature distribution and more accurately represent ventilation cooling. This requires representing the 3D ventilation geometry in a 2D model by accounting for additional surface areas and enhanced convective heat transfer. This chapter reviews established approaches in line with the aim of this thesis. These approaches are categorized into two groups, approach 1 and 2.

2.4.1 Approach 1: Flattened section view model

The first approach formulates the 2-D model in the Cartesian coordinate system, with computation done at the rotor radius of interest and flattened to a 2D plane (Sheridan et al., 1988). Figure 9 illustrates a vented rotor model with symmetry lines for the airflow passage and cooling web, also called vent and vane. The lower half of the figure displays the 2D geometry model used in the analysis, simplified by exploiting symmetry.

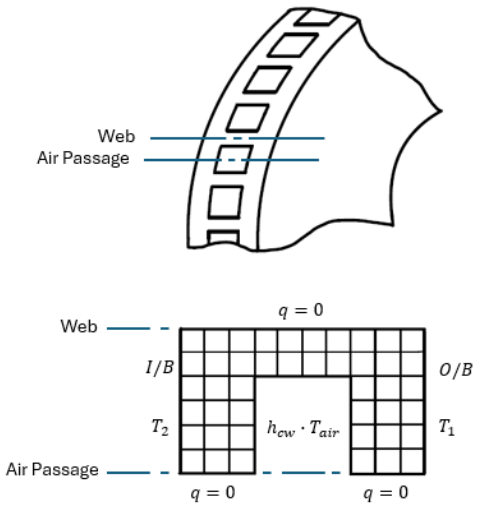

Figure 9: Schematic diagram of the vented rotor. Adopted from (Sheridan et al., 1988)

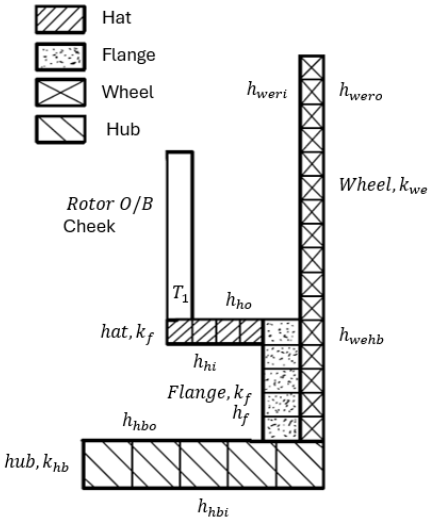

Figure 10: Schematic diagram of the hat model. Adopted from (Sheridan et al., 1988)

As shown, the convective heat transfer coefficient h_{cw} is applied to the vented edges, while O/B and I/B refer to the two surfaces of the friction ring with heat input. Edge O/B's boundary condition is corrected to include the cooling and conduction of the rotor hat section, which is otherwise missed from the model. This correction is performed using a 1D FE model of the hat section, see figure 10.

Modeling convection and radiation from the outer and inner mantle areas of the 3D brake disc is difficult with this 2D model approach. However, their impact on the 2D temperature field and friction ring temperature should be small in relation to the cooling effect of the vents. Therefore, neglecting it or applying correction factor to edges O/B and I/B, as done for the O/B hat contribution, can be a valid approach.

2.4.2 Approach 2: Axisymmetric model

The second approach formulates an axisymmetric 2D model using a cross-sectional view through thickness cut of the disc, illustrated in Figure 11. Lee and Yeo propose a numerical technique that uses homogenization to represent the combined vents and vanes by assigning equivalent thermal properties on the ventilation layer bulk surface, along with convection heat transfer boundary condition (Lee & Yeo, 2000).

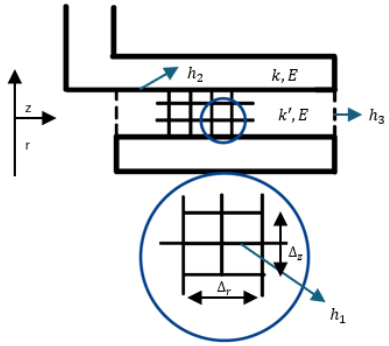

Figure 11: Equivalent thermal properties. Adapted from (Lee & Yeo, 2000)

Where h_1 is the equivalent heat transfer coefficients for the element faces of the vent holes, h_2 the vent walls parallel to the frictional surface, and h_3 the rotor's inner and outer diameter surface. These are expressed in terms of h_v, the vent wall's heat transfer coefficient, ensuring that the total heat loss must remain the same in the axisymmetric model.

By balancing heat loss in the 2D and 3D model h_1 is found,

$$2\pi(\Delta r)h_1(T - T_\infty) = 2n(\Delta r)(\Delta z)h_v(T - T_\infty) \tag{9}$$

Where n is the number of vent holes, 2 accounts for the two surfaces of each vent and Δr, Δz are element lengths in the radial and axial directions. Solving for h_1 gives,

$$h_1 = \frac{n(\Delta z)h_v}{\pi r} \tag{10}$$

Similarly,

$$h_2 = \frac{\emptyset_v}{2\pi}h_v,\ h_3 = \frac{2\pi - \emptyset_v}{2\pi}h_h \tag{11}$$

Where $\emptyset_v$ is the total angle that the vent holes occupy and h_h is the heat transfer coefficient at the rotors inner and outer diameter, which is different from h_v.

The thermal conductivity in the ventilation layer is modified into equivalently as,

$$k' = \frac{2\pi - \emptyset_v}{2\pi}k \tag{12}$$

2.4.3 Comparison of different approaches

Both approaches effectively capture out-of-plane temperature distribution as well as the temperature at the friction surface, which is the primary interest of the analysis. The approaches demonstrate improved accuracy in modeling ventilation cooling and show close correlation to a reference model, as evidenced by the reports.

Approach 1 captures temperature variation through the disc thickness in the axial direction, making it suitable for identifying hot spots within disc brake geometry. Whereas approach 2 captures temperature variation through the thickness in the radial direction, which is useful for analyzing such as coning deformation of the brake disc. Each model has its merit, with the choice of approach depending on the specific analysis objective.

2.4.4 Choice of approach

After reviewing the different choices, it was decided to develop a new approach instead of following a previously established one. The new approach will be similar to approach 2, but instead of scaling the conduction and convection coefficients based on the percentage of the vent size, the new approach will scale the terms in the weak form by integrating the terms over their size in the out-of-plane direction.

3. Enriched axisymmetric model

3.1 Geometry

Description of the geometry of the brake rotor and how it is converted from 3D to 2D without losing the proportions and out-of-plane surfaces.

3.1.1 Idealization of geometry

In ventilated brake discs, there is a ventilation layer in the middle for improved cooling by introducing airflow inside the disc as can be seen in Figure 12. The ventilation layer mostly consists of air, but it still has solid material in the form of vanes, separating the ventilation layer into many different vents. This layer is the reason why the model is not fully axisymmetric, however in the 3D model the layer is pattern axisymmetric.

Figure 12: Ventilation layer in 3D model

The model geometry is defined in a cylindrical coordinate system with the dimensions r [m], z [m] and φ [rad]. This is done because the model is going to be converted into 2D with asymmetry around the φ-axis, as seen in Figure 13.

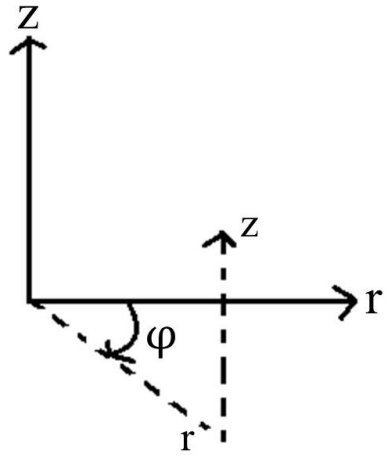

Figure 13: Coordinate system

When converting the model from 3 dimensions to 2 dimensions many of the features cannot be converted or will make the geometry unnecessarily complicated with only a minimal effect on the result. Therefore, the rounded edges and the mounting holes were removed. The rounded edges on the vanes were removed because they could not be captured in the 2D model, but the effect of the difference in the amount of material is negligible. In 3D the model the vanes are straight and have a uniform width and the vents have the form of a circle sector like what is referred to a “pie slice” in this report.

Performing a geometry mapping of the volumes and surfaces of the vanes becomes very complicated when their width is constant in distance (measured in millimeters) in a cylindrical coordinate system. To make the mapping less complicated the width of the vanes were simplified to be in radians instead. The simplifications can be viewed in Figure 14.

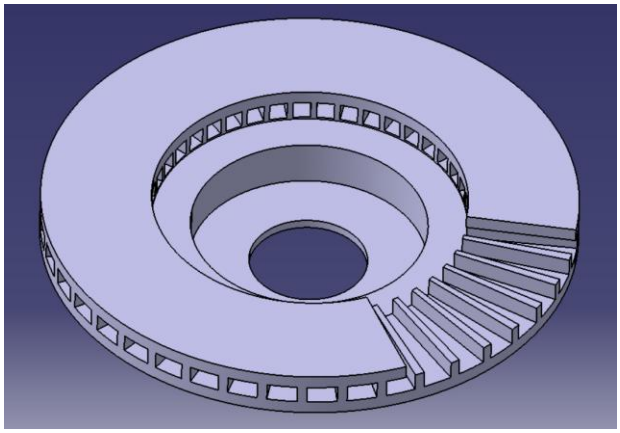

Figure 14: Simplified 3D model

However, this makes the vanes "pie shaped like the vent, meaning that they get thicker the further from the center they get. A comparison of vanes in the ventilation layer between a 3D model and a simplified model is shown in Figure 15. To compensate for this the angle is measured at the centre of the vanes in r-direction as seen in Figure 16, which means that the material loss at the inner radius gets added at the outer radius. Meaning that the total amount of material in the vent layer remains about the same, which should give an accurate approximation.

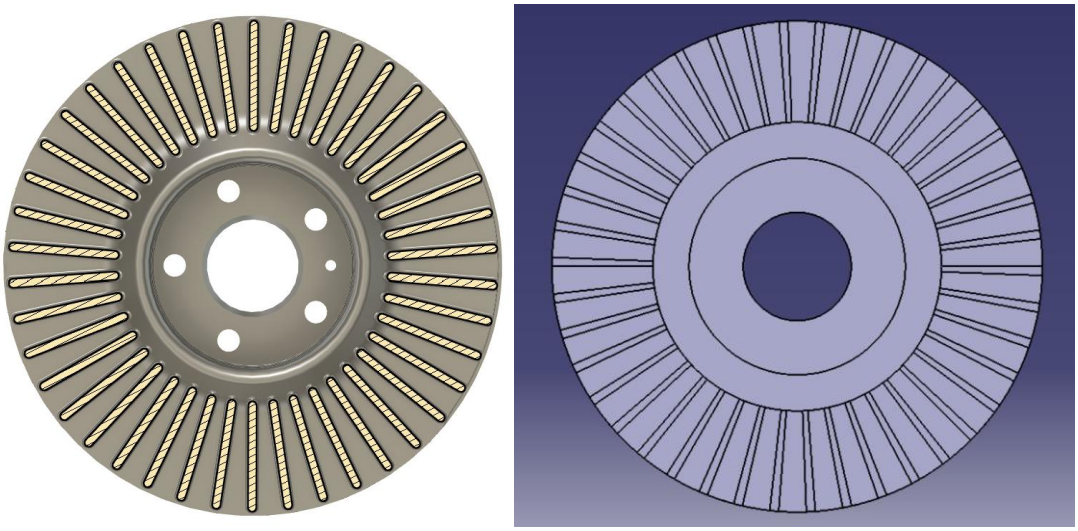

Figure 15: Vent layer comparison between 3D model and approximation

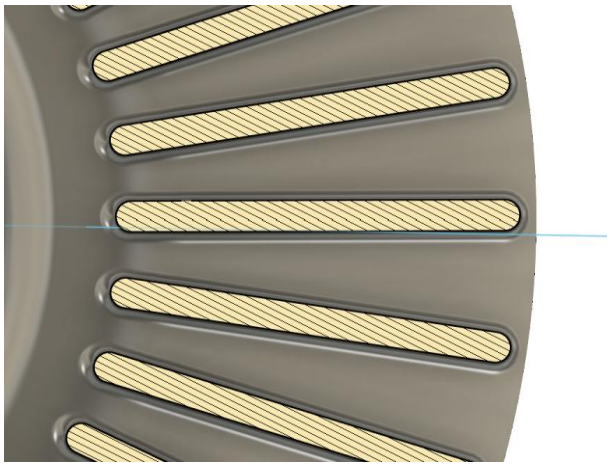

Figure 16: Zoom in on vane with angle measurement

In the 2D enriched model the important factors are the total angle of the vent layer that consists of solid material and the vent layers total surface area. Therefore, before converting the model from 3D all vanes can be combined into one big vane to make the geometry mapping easier in the next section (see Figure 17). The total combined width of the vents in radians is denoted as β and calculated in eq. 13.

$$\beta = n * \gamma \tag{13}$$

Where n is the number of vents and γ the width of the vents in radians. Each of the vanes that gets combined have two surfaces that get lost in the conversion and must be added on to the combined vane represented on volume 5 in Figure 18. The total area that is projected is determined in eq. 14.

$$A_v = n[A_{VL} + A_{VR}] \tag{14}$$

Where A_v is the total surface area that gets lost, n is the total number of vents, and A_{VL} and A_{VR} are the vertical surface area of the left and right side of a singular vane.

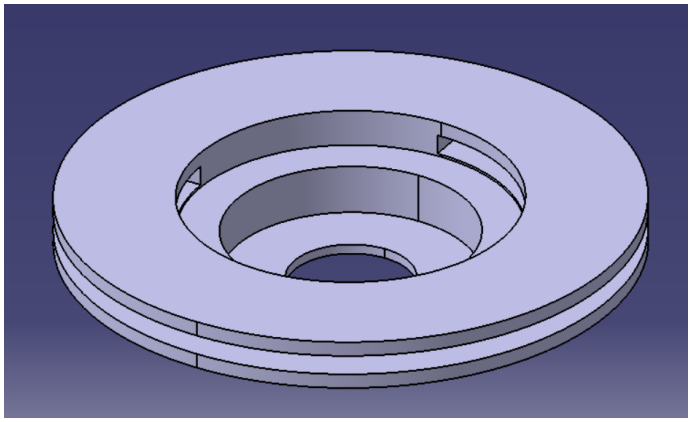

Figure 17: Further simplified model with combined vent

A cross-section view of the brake rotor can be seen in Figure 18, with denoted volumes and surfaces. The only volume that is not fully axisymmetric around the φ-axis is V5, since the vent layer is made up of one section of solid material and one section of air. The surfaces A15, A16, A19 and A22 are connected to the vent layer and are because of this not axisymmetric. The surfaces A15 and A19 are the horizontal top and bottom surfaces of the vent layer, these surfaces are important to

capture accurately because of the high convection from the air flow through the vent. The same is true for the left and right vertical wall surfaces, AVL and AVR, in the vents. The surfaces A16 and A22 are the mantle surfaces of the solid part of the vent layer and the area for convection and radiation will be greatly reduced. It is important to capture the true area of these surfaces to accurately model the convection.

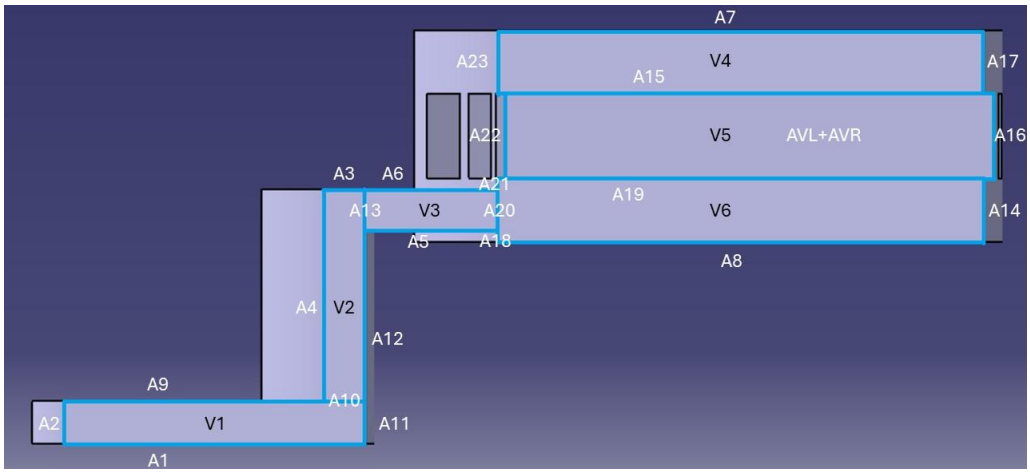

Figure 18: 2D view of disc with denoted faces and edges

3.1.2 Geometry mapping

When converting from 3D to a 2D enriched model it is important to keep track of the length of geometry feature in the dimension that disappears. This is because the brake disc is not fully axisymmetric and does not have the same length on all surfaces and volumes in the φ-direction. With different lengths in the out of plane direction the 2D model must have their corresponding edges and faces weighted based on these proportions. To accomplish this all the volumes and surfaces had to have their coordinates mapped. The dimension of the model can be seen in Figure 19.

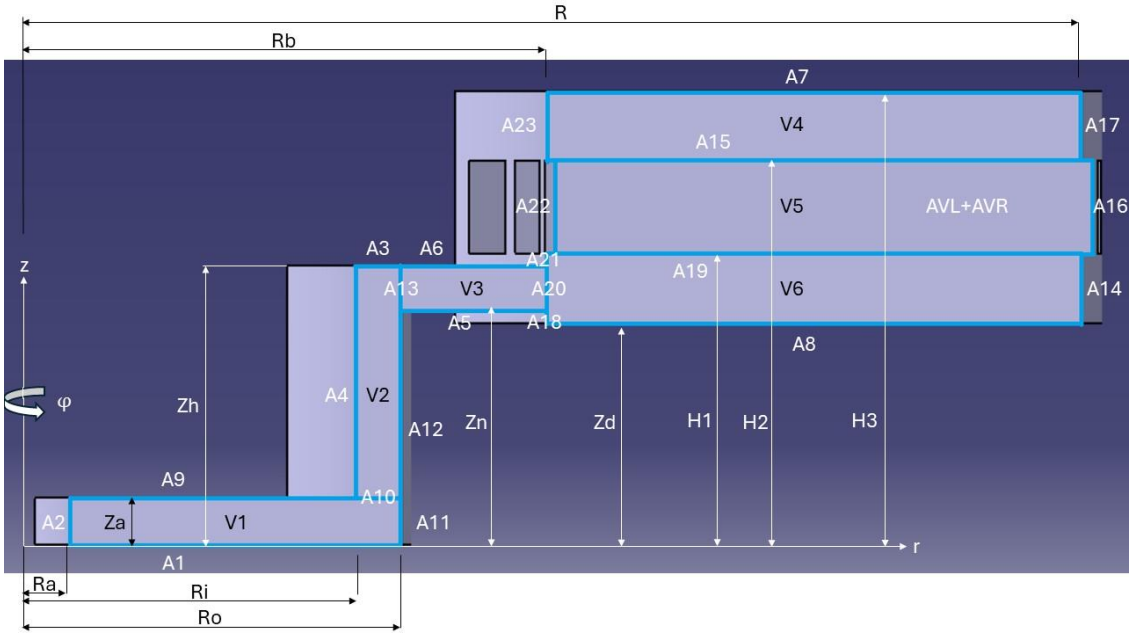

Figure 19: Cross-section view with denoted dimensions

β – total vent width

$n - number\ of\ vents$

$\gamma - width\ of\ vent\ in\ radians$

$\theta - area\ in\ radians\ where\ heat\ is\ supplied\ from\ brakes$

Surfaces:

$$A_1 = \{R_a < r < R_o, 0 < \varphi < 2\pi, z = 0\}\ dS = rd\varphi dr$$
$$A_2 = \{r = R_a, 0 < \varphi < 2\pi, 0 < z < z_a\}\ dS = rd\varphi dz$$
$$A_3 = \{R_i < r < R_o, 0 < \varphi < 2\pi, z = z_h\}\ dS = rd\varphi dr$$
$$A_4 = \{r = R_i, 0 < \varphi < 2\pi, z_a < z < z_h\}\ dS = rd\varphi dz$$
$$A_5 = \{R_0 < r < R_b, 0 < \varphi < 2\pi, z = z_n\}\ dS = rd\varphi dr$$
$$A_6 = \{R_0 < r < R_b, 0 < \varphi < 2\pi, z = z_h\}\ dS = rd\varphi dr$$
$$A_7 = \{R_b < r < R, 0 < \varphi < 2\pi, z = H_3\}\ dS = rd\varphi dr$$
$$A_8 = \{R_b < r < R, 0 < \varphi < 2\pi, z = z_d\}\ dS = rd\varphi dr$$
$$A_9 = \{R_a < r < R_i, 0 < \varphi < 2\pi, z = z_a\}\ dS = rd\varphi dr$$
$$A_{11} = \{r = R_o, 0 < \varphi < 2\pi, 0 < z < z_a\}\ dS = rd\varphi dz$$
$$A_{12} = \{r = R_0, 0 < \varphi < 2\pi, z_a < z < z_n\}\ dS = rd\varphi dz$$
$$A_{14} = \{r = R, 0 < \varphi < 2\pi, z_d < z < H_1\}\ dS = rd\varphi dz$$
$$A_{15} = \{R_b < r < R, 0 < \varphi < \beta, z = H_2\}\ dS = rd\varphi dr$$
$$A_{16} = \{r = R, \beta < \varphi < 2\pi, H_1 < z < H_2\}\ dS = rd\varphi dz$$
$$A_{17} = \{r = R, 0 < \varphi < 2\pi, H_2 < z < H_3\}\ dS = rd\varphi dz$$
$$A_{18} = \{r = R_b, 0 < \varphi < 2\pi, z_d < z < z_n\}\ dS = rd\varphi dz$$
$$A_{19} = \{R_b < r < R, 0 < \varphi < \beta, z = H_1\}\ dS = rd\varphi dr$$
$$A_{21} = \{r = R_b, 0 < \varphi < 2\pi, z_h < z < H_1\}\ dS = rd\varphi dz$$
$$A_{22} = \{r = R_b, \beta < \varphi < 2\pi, H_1 < z < H_2\}\ dS = rd\varphi dz$$
$$A_{23} = \{r = R_b, 0 < \varphi < 2\pi, H_2 < z < H_3\}\ dS = rd\varphi dz$$

Vertical convection surfaces in ventilation layer:

$$A_{VL} = n\{R_b < r < R, \varphi = \beta, H_1 < z < H_2\}\ dS = ndrdz$$
$$A_{VR} = n\{R_b < r < R, \varphi = 0, H_1 < z < H_2\}\ dS = ndrdz$$

Where A_{VL} and A_{VR} are the vertical surface area of left and right side of the vanes respectively, and n is the number of vanes since it is the vertical surface area of all combined.

Volumes:

$$V_1 = \{R_a < r < R_o, 0 < \varphi < 2\pi, 0 < z < z_a\} = \{(r, z) \in \Omega_1, \varphi \in (0, 2\pi)\}\ dV = rd\varphi drdz = rd\varphi d\Omega$$
$$V_2 = \{R_i < r < R_0, 0 < \varphi < 2\pi, z_a < z < z_h\} = \{(r, z) \in \Omega_2, \varphi \in (0, 2\pi)\}\ dV = rd\varphi drdz = rd\varphi d\Omega$$
$$V_3 = \{R_o < r < R_b, 0 < \varphi < 2\pi, z_n < z < z_h = \{(r, z) \in \Omega_3, \varphi \in (0, 2\pi)\}\}\ dV = rd\varphi drdz = rd\varphi d\Omega$$
$$V_4 = \{R_b < r < R, 0 < \varphi < 2\pi, H_2 < z < H_3\} = \{(r, z) \in \Omega_4, \varphi \in (0, 2\pi)\}\ dV = rd\varphi drdz = rd\varphi d\Omega$$
$$V_5 = \{R_b < r < R, \beta < \varphi < 2\pi, H_1 < z < H_2\} = \{\{r, z\} \in \Omega_5, \varphi \in (\beta, 2\pi)\}\ dV = rd\varphi drdz = rd\varphi d\Omega$$
$$V_6 = \{R_b < r < R, 0 < \varphi < 2\pi, z_d < z < H_1\} = \{(r, z) \in \Omega_6, \varphi \in (\beta, 2\pi)\}\ dV = rd\varphi drdz = rd\varphi d\Omega$$

4.1.3 Conversion to enriched 2D axisymmetric model

The simplified 3D model is converted to an enriched 2D axisymmetric model, where the volumes are transformed to faces and the surfaces to edges, as can be seen in Figure 20.

Since the ventilation layer consists of both solid material and convection surfaces, F5 represents both volume and area:

$$F5 = \{V_5 \cup A_{VL} \cup A_{VR}\}$$

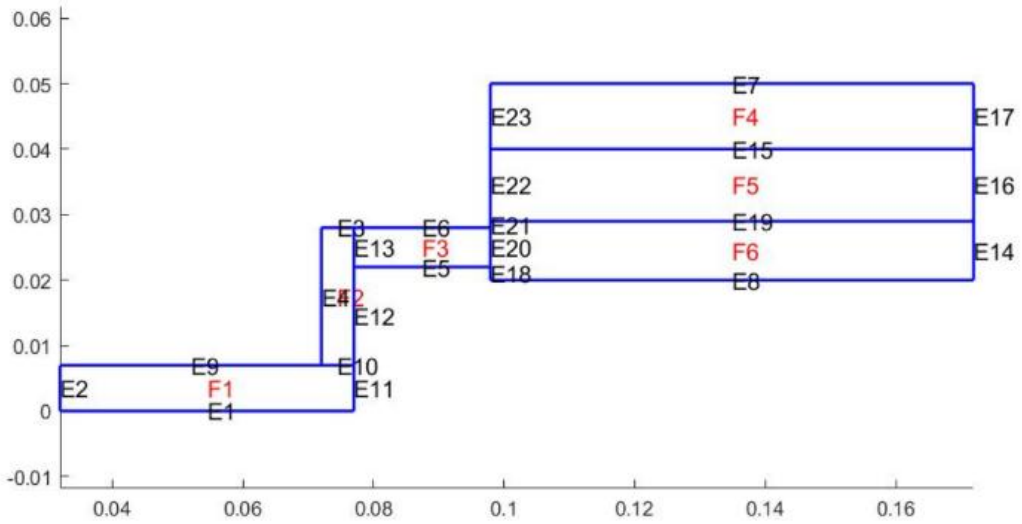

Figure 20: 2D enriched axisymmetric model

3.1.4 Surface and volume grouping

To make the process of deriving the weak- and FE-form less demanding the surfaces and volumes were combined into groups based on boundary conditions and coordinates. Edges that shared the same φ-coordinates and properties can be grouped together to reduce the number of terms to keep track of when deriving the equations. The process can be repeated for the faces using the same logic. On the friction ring edges there are heat outflux from the friction heat and there occurs heat energy loss from radiation, but there is no convection due to the proximity of the brake pad blocking the air flow.
The heat outflux from the friction heat get added on the friction ring from braking, it also occurs energy loss from radiation here. But no energy loss from convection due to the proximity of the brake pad restricting the air flow.
The surfaces inside the ventilation layer are modeled as only having heat loss from convection, not from radiation due to the electromagnetic waves getting mostly trapped inside the vents.

Edges with convection: E1, E3, E4, E5, E6, E9, E11, E12, E14, E15, E16, E17, E18, E19, E21, E22 and E23

Edges with radiation: E1, E3, E4, E5, E6, E7, E8, E9, E11, E12, E14, E16, E17, E18, E21, E22 and E23

Edges with heat outflux: E7 and E8

Edges grouped based on having the same φ-coordinates and boundary conditions:

$$A_{rc} = \{E1 \cup E9 \cup E11 \cup E12 \cup E4 \cup E14 \cup E3 \cup E6 \cup E5 \cup E20 \cup E22 \cup E24 \cup E16 \cup E18\}$$

$$A_b = \{E7 \cup E8\}$$

$$A_{HC} = \{E15 \cup E19\}$$
$$A_{VC} = \{E17 \cup E23\}$$
$$A_v = \{nA_{VL} \cup nA_{VH}\}$$

Where A_b is the friction ring surfaces, A_{HC} is the horizontal convection surfaces inside the vent, A_{VC} is the mantle area of the vent and A_{rc} is the rest of the surfaces with φ between 0 and 2π.

The process was repeated for the volumes:

$$V_s = \{F1 \cup F2 \cup F3 \cup F4 \cup F6\}$$
$$V_v = F5$$

where V_v represents the ventilation layer. The edge and face groupings are shown in Figure 21 where each grouping is represented by a color.

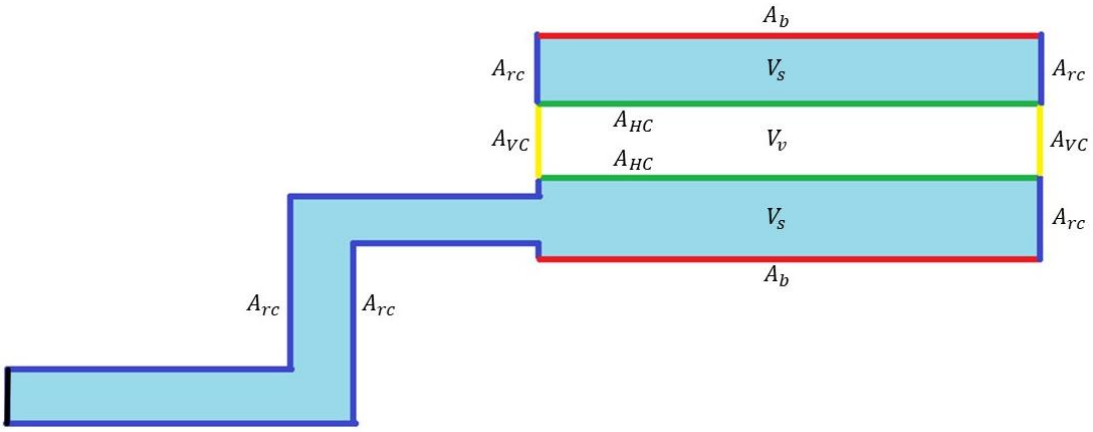

Figure 21: 2D view of model with groupings shown in colour

3.2 Finite Element Analysis

The temperature over the geometry in time and space are expressed as partial differential equations that are too complex to be solved analytically. Therefore, an approximation of the partial differential equations must be constructed using discretization. This discretized model is approximated as numerical model equations, solved with numerical methods. The finite element method is used to solve these approximate numerical model equations of the partial differential equations. The result of this method will also be an approximation of the result of the partial differential equations.
(COMSOL Multiphysics, 2017)

3.2.1 Parameters

Important parameters to solve the transient heat problem and how to implement them into the governing equation.

3.2.1.1 Friction heat

Data from an AMS test on the total power (Watt) applied to the entire brake disc in each time step are provided by VCC. The data is applied as W/m^2 in the model and gotten from dividing the total power by the friction surface of the ring.

3.2.2 Strong Form

The strong form consists of the governing differential equation and boundary conditions. In this case the governing differential equation is the heat equation, and the boundary conditions consists of heat outflux, convection and radiation. Since the brake disc is modeled as a transient heat flow problem, an initial temperature condition is necessary.

To avoid having to write (r, z) in every equation we write it as $\boldsymbol{x} = (r, z)$ instead

$r\rho_d c_d \dot{T} + \nabla^T[rq(\nabla T)] = rQ$	in $\Omega \times [0, t_{tot}]$	(Heat equation)
$q_n(\boldsymbol{x}, t) = q_b(\boldsymbol{x}, t)$	on $\Gamma_h \times [0, t_{tot}]$	(Heat outflux)
$q_n(\boldsymbol{x}, t) = h_c(\boldsymbol{x}, t)[T(x, t) - T_\infty]$	on $\Gamma_c \times [0, t_{tot}]$	(Convection)
$q_n(\boldsymbol{x}, t) = h_r(\boldsymbol{x}, t) = \varepsilon_e \sigma[T^4 - T_\infty^4]$	on $\Gamma_r \times [0, t_{tot}]$	(Radiation)
$T(\boldsymbol{x}, 0) = T_0(\boldsymbol{x})$,	$x \in \Omega$	(Initial condition)

r – radial coordinate	[m]
ρ_d – density of the disc	[kg/m^3]
c_d – mass specific heat capacity of the disc	[J/(kgK)]
$\dot{T}$ – temperature change per second	[°C/s]
$\nabla^T = \left[\frac{d}{dr} \quad \frac{d}{dz}\right]$	
Q – distributed heat source	[W/m^3]
q_n - heat outflux	[W/m^2]
q_b - heat flux from braking	[W/m^2]
h_c – convection coefficient	[W/(m^{2}K)]
T_∞ - ambient temperature	[°C]
T_0 – initial temperature	[°C]

3.2.3 Weak form

To obtain the weak form the governing equation was multiplied by the arbitrary test function w(x). To convert the model to 2D the governing differential equation was integrated first over the 2D domain and then over phi. Where the length of the φ-direction becomes a weight factor for how much each surface or volume contributes to the heat problem.

$$\int_{\varphi}\int_{\Omega} w(\boldsymbol{x}) r \rho_d c_d \dot{T} d\Omega d\varphi + \int_{\varphi}\int_{\Omega} w(\boldsymbol{x}) \boldsymbol{\nabla}^T [r\boldsymbol{q}(\boldsymbol{x})] d\Omega d\varphi = \int_{\varphi}\int_{\Omega} w(\boldsymbol{x}) r Q d\Omega d\varphi \quad (15)$$

Green-Gauss divergence theorem was used on the vector function $\mathbf{q}(\mathbf{x})$ and scalar function w(x) to implement the boundary conditions into the equation:

$$\int_{\Omega} w(\boldsymbol{x}) \boldsymbol{\nabla}^T [r\boldsymbol{q}(\boldsymbol{x})] d\Omega = \int_{\Gamma} w(\boldsymbol{x}) r \boldsymbol{q}^t \boldsymbol{n} d\Gamma - \int_{\Omega} \boldsymbol{\nabla}^T [w(\boldsymbol{x})] r \boldsymbol{q}(\boldsymbol{x}) d\Omega \quad (16)$$

Eq. 16 was inserted into eq. 15 ⇒

$$\int_{\varphi}\int_{\Omega} w(\boldsymbol{x}) r \rho_d c_d \dot{T} d\Omega d\varphi + \int_{\varphi}\int_{\Gamma} w(\boldsymbol{x}) r \boldsymbol{q}^T \boldsymbol{n} d\Gamma d\varphi - \int_{\varphi}\int_{\Omega} [\boldsymbol{\nabla} w(\boldsymbol{x})]^T r \boldsymbol{q} d\Omega d\varphi = \int_{\varphi}\int_{\Omega} r w(\boldsymbol{x})\, Q d\Omega d\varphi \quad (17)$$

The heat flux vector q is determined from Fourier's law for an isotropic material,

$$\boldsymbol{q} = -\boldsymbol{D}[\boldsymbol{\nabla} T] \quad (18)$$

where D is determined by $\boldsymbol{D} = k_{cond}\boldsymbol{I}$ where k_{cond} is the thermal conductivity of the material and $\boldsymbol{I}$ is the identity matrix. When eq. 18 is inserted into eq. 17, we get:

$$\int_{\varphi}\int_{\Omega} w(\boldsymbol{x}) r \rho_d c_d \dot{T} d\Omega d\varphi + \int_{\varphi}\int_{\Omega} [\boldsymbol{\nabla} w(\boldsymbol{x})]^T r \boldsymbol{D} [\boldsymbol{\nabla}^T T] d\Omega d\varphi = \int_{\varphi}\int_{\Omega} r w(\boldsymbol{x}) Q d\Omega d\varphi - \int_{\varphi}\int_{\Gamma} w(\boldsymbol{x}) r \boldsymbol{q}_n d\Gamma d\varphi \quad (19)$$

Since the vent layer has different properties, the total domain can effectively be separated into two smaller domains differently weighted. This was done by separating the domain based on the volume grouping and integrating over their corresponding φ-coordinates.

$$V_s: \int_{0}^{2\pi}\int_{\Omega_s} w(\boldsymbol{x}) r \rho_d c_d \dot{T}\, d\Omega d\varphi + \int_{0}^{2\pi}\int_{\Omega_s} w(\boldsymbol{x}) \boldsymbol{\nabla}^T [r\boldsymbol{q}(\boldsymbol{\nabla} T)]\, d\Omega d\varphi = \int_{0}^{2\pi}\int_{\Omega_s} r w(\boldsymbol{x}) Q d\Omega d\varphi - \int_{0}^{2\pi}\int_{\Gamma} w(\boldsymbol{x}) r q_n d\Gamma d\varphi \quad (20)$$

$$V_v: \int_{\beta}^{2\pi}\int_{\Omega_v} w(\boldsymbol{x})\, r \rho_d c_d \dot{T} d\Omega d\varphi + \int_{\beta}^{2\pi}\int_{\Omega_v} w(\boldsymbol{x}) \boldsymbol{\nabla}^T [r q(\boldsymbol{\nabla} T)]\, d\Omega d\varphi = \int_{\beta}^{2\pi}\int_{\Omega_v} r w(\boldsymbol{x}) Q d\Omega d\varphi - \int_{\beta}^{2\pi}\int_{\Gamma} w(\boldsymbol{x}) r \boldsymbol{q}_n d\Gamma d\varphi \quad (21)$$

Ω_s – 2D domain made up of face F_1, F_2, F_3, F_4 and F_6
Ω_v – 2D domain made up of face F_5

Combine eq. 20 and 21 into the same weak form because together they make up the total domain.

$$\int_0^{2\pi}\int_{\Omega_s} w(\boldsymbol{x})r\rho_d c_d\dot{T}d\Omega d\varphi + \int_\beta^{2\pi}\int_{\Omega_v} w(\boldsymbol{x})r\rho_d c_d\dot{T}d\Omega d\varphi + \int_0^{2\pi}\int_{\Omega_s} [\boldsymbol{\nabla}w(\boldsymbol{x})]^T r\boldsymbol{D}[\boldsymbol{\nabla}^T T]d\Omega d\varphi$$
$$+ \int_\beta^{2\pi}\int_{\Omega_v} [\boldsymbol{\nabla}w(\boldsymbol{x})]^T r\boldsymbol{D}[\boldsymbol{\nabla}^T T]d\Omega d\varphi = \int_\varphi\int_\Omega rw(\boldsymbol{x})Qd\Omega d\varphi - \int_\varphi\int_\Gamma w(\boldsymbol{x})r\boldsymbol{q}_n d\Gamma d\varphi \qquad (22)$$

The boundary term was also separated based on the previously developed edge groupings and their boundary terms were integrated over the corresponding boundaries and φ-coordinates.

$$\int_\varphi\int_\Gamma w(\boldsymbol{x})r\boldsymbol{q}_n d\Gamma d\varphi =$$
$$= \int_0^{2\pi}\int_{\Gamma_{rc}} [w(\boldsymbol{x})rh_c[T-T_\infty] + w(\boldsymbol{x})rh_r(\boldsymbol{x},t)]d\Gamma d\varphi + \int_0^{\theta}\int_{\Gamma_b} w(\boldsymbol{x})rq_b d\Gamma d\varphi$$
$$+ \int_0^{2\pi}\int_{\Gamma_b} w(\boldsymbol{x})rh_r(\boldsymbol{x},t)d\Gamma d\varphi + \int_0^{\beta}\int_{\Gamma_{HC}} w(\boldsymbol{x})rh_c[T-T_\infty]d\Gamma d\varphi$$
$$+ \int_\beta^{2\pi}\int_{\Gamma_{vc}} [w(\boldsymbol{x})rh_c[T-T_\infty] + w(\boldsymbol{x})rh_r(\boldsymbol{x},t)]d\Gamma d\varphi \qquad (23)$$

Γ_{rc} – boundary made up of edges E_1, E_3, E_4, E_5, E_6, E_9, E_{11}, E_{12}, E_{14}, E_{17}, E_{18}, E_{21} and E_{23}
Γ_b – boundary made up of edges E_7 and E_8
Γ_{HC} – boundary made up of edges E_{15} and E_{19}
Γ_{VC} – boundary made up of edge E_{16} and E_{22}

The next step was to insert eq. 22 into eq. 23. Since there is no distributed inner heat source, Q is 0, the corresponding term in the weak form is zero.

$$2\pi\int_{\Omega_s} w(\boldsymbol{x})r\rho_d c_d\dot{T}d\Omega + [2\pi-\beta]\int_{\Omega_v} w(\boldsymbol{x})r\rho_d c_d\dot{T}d\Omega + 2\pi\int_{\Omega_s} [\boldsymbol{\nabla}w(\boldsymbol{x})]^T r\boldsymbol{D}[\boldsymbol{\nabla}^T T]d\Omega$$
$$+ [2\pi-\beta]\int_{\Omega_v} [\boldsymbol{\nabla}w(\boldsymbol{x})]^T r\boldsymbol{D}[\boldsymbol{\nabla}^T T]d\Omega + 2\pi\int_{\Gamma_{rc}} w(\boldsymbol{x})rh_c T d\Gamma + \beta\int_{\Gamma_{HC}} w(\boldsymbol{x})rh_c T d\Gamma d\varphi$$
$$+ [2\pi-\beta]\int_{\Gamma_{vc}} [w(\boldsymbol{x})rh_c T]d\Gamma d\varphi$$
$$= 2\pi\int_{\Gamma_{rc}} w(\boldsymbol{x})rh_c T_\infty d\Gamma - \theta\int_{\Gamma_b} w(\boldsymbol{x})rq_b d\Gamma + \beta\int_{\Gamma_{HC}} w(\boldsymbol{x})rh_c T_\infty d\Gamma$$
$$- [2\pi-\beta]\int_{\Gamma_{vc}} w(\boldsymbol{x})rh_c T_\infty d\Gamma$$
$$+ [2\pi-\beta]\int_{\Gamma_{vc}} w(\boldsymbol{x})rh_r(\boldsymbol{x},t)d\Gamma - 2\pi\int_{\Gamma_{rc}\cup\Gamma_b} w(\boldsymbol{x})rh_r(\boldsymbol{x},t)d\Gamma \qquad (24)$$

In the current weak form the convection contribution from the surfaces along the vanes is not included and must be added onto Ω_v.

$$2n \int_{\Omega_v} w(\boldsymbol{x}) h_c [T - T_\infty] d\Omega \tag{25}$$

Add equation 25 to equation 24 $\Rightarrow$

$$\begin{aligned}
&2\pi \int_{\Omega_s} w(\boldsymbol{x}) r \rho_d c_d \dot{T} d\Omega + [2\pi - \beta] \int_{\Omega_v} w(\boldsymbol{x}) r \rho_d c_d \dot{T} d\Omega + 2\pi \int_{\Omega_s} [\boldsymbol{\nabla} w(\boldsymbol{x})]^T r \boldsymbol{D} [\boldsymbol{\nabla}^T T] d\Omega \\
&\quad + [2\pi - \beta] \int_{\Omega_v} [\boldsymbol{\nabla} w(\boldsymbol{x})]^T r \boldsymbol{D} [\boldsymbol{\nabla}^T T] d\Omega + 2n \int_{\Omega_v} w(\boldsymbol{x}) h_c [T] d\Omega + 2\pi \int_{\Gamma_{rc}} w(\boldsymbol{x}) r h_c T d\Gamma \\
&\quad + \beta \int_{\Gamma_{HC}} w(\boldsymbol{x}) r h_c T d\Gamma + [2\pi - \beta] \int_{\Gamma_{vc}} w(\boldsymbol{x}) r h_c T d\Gamma \\
&\quad + [2\pi - \beta] \int_{\Gamma_{vc}} w(\boldsymbol{x}) r h_r(\boldsymbol{x}, t) d\Gamma + 2\pi \int_{\Gamma_{rc} \cup \Gamma_b} w(\boldsymbol{x}) r h_r(\boldsymbol{x}, t) d\Gamma \\
&\quad = 2n \int_{\Omega_v} w(\boldsymbol{x}) h_c T_\infty d\Omega + 2\pi \int_{\Gamma_{rc}} w(\boldsymbol{x}) r h_c T_\infty d\Gamma - \theta \int_{\Gamma_b} w(\boldsymbol{x}) r q_b d\Gamma \\
&\quad + \beta \int_{\Gamma_{HC}} w(\boldsymbol{x}) r h_c T_\infty d\Gamma + [2\pi - \beta] \int_{\Gamma_{vc}} w(\boldsymbol{x}) r h_c T_\infty d\Gamma
\end{aligned} \tag{26}$$

To be able to solve equation 26, it must be included that the time step $T(x, 0)$ is equal to the initial temperature from the AMS test, see eq. 27,

$$T(x, 0) = T_0(x) \tag{27}$$

3.2.4 FE-form

The next step is to perform a spatial discretization of the weak form. To accomplish this the continuous spatial domain is discretized into a finite number of elements defined by corresponding nodes.

The temperature is approximated to:

$$T(\boldsymbol{x}, t) \approx T_h = \boldsymbol{N}(\boldsymbol{x}) \boldsymbol{a}(t) \tag{28}$$

were

$$\boldsymbol{N}(\boldsymbol{x}) = [N_1(\boldsymbol{x}) \quad N_2(\boldsymbol{x}) \quad \cdots \quad N_n(\boldsymbol{x})]$$

is the row-matrix of n nodal shape functions and

$$\boldsymbol{a}(t) = [a_1(t) \quad a_2(t) \quad \cdots \quad a_n(t)]$$

is the nodal temperature vector. It should be noted that $\mathbf{N}(\mathbf{x})$ is a function of $\mathbf{x}$ and $\mathbf{a}(t)$ is a function of time, meaning that the time dependence of T_h is carried by $\mathbf{a}(t)$ and the spatial variation is carried by $\mathbf{N}(\mathbf{x})$.

To get the derivative of $\mathbf{T}_h$ with respect to $\mathbf{x}$, $\boldsymbol{\nabla} = \left[\frac{d}{dr} \quad \frac{\delta}{dz}\right]^T$ is used.

$$\nabla T_h = \nabla[\boldsymbol{N}(\boldsymbol{x})\boldsymbol{a}(t)] = [\nabla \mathbf{N}(\boldsymbol{x})]\boldsymbol{a}(t) = \boldsymbol{B}(x)\boldsymbol{a}(t) \tag{29}$$

$$\boldsymbol{B}(\boldsymbol{x}) = \nabla \boldsymbol{N} = \begin{bmatrix} \frac{dN_1}{dr} & \frac{dN_2}{dr} & \cdots \frac{dN_n}{dr} \\ \frac{dN_1}{dz} & \frac{dN_2}{dz} & \cdots \frac{dN_n}{dz} \end{bmatrix}$$

To get the time derivative of T_h:

$$\dot{T}_h = \frac{d[\boldsymbol{N}(\boldsymbol{x})\boldsymbol{a}(t)]}{dt} = \boldsymbol{N}(\boldsymbol{x})\dot{\boldsymbol{a}}(t) \tag{30}$$

In the next step w(**x**) is discretized, in accordance with the Galerkin method, with the same shape functions.

$$w(\boldsymbol{x}) = w_h(\boldsymbol{x}) = \boldsymbol{N}(\boldsymbol{x})\boldsymbol{c} \tag{31}$$

Where **c** is a vector of arbitrary coefficients (virtual nodal temperature). With the relations:

$$w_h^T = [\boldsymbol{N}\boldsymbol{c}]^T = \boldsymbol{c}^T\boldsymbol{N}^T \tag{32}$$

$$[\nabla w_h]^T = [\boldsymbol{B}\boldsymbol{c}]^T = \boldsymbol{c}^T\boldsymbol{B}^T \tag{33}$$

Substitute w(**x**) and T_h with previously stated equations 28, 29, 30, 32 and 33 into the weak form (eq. 26).

$$\begin{aligned}
&2\pi \int_{\Omega_s} \boldsymbol{c}^T\boldsymbol{N}^T r\rho_d c_d \boldsymbol{N}\dot{\boldsymbol{a}} d\Omega + [2\pi - \beta] \int_{\Omega_v} \boldsymbol{c}^T\boldsymbol{N}^T r\rho_d c_d \boldsymbol{N}\dot{\boldsymbol{a}} d\Omega + 2\pi \int_{\Omega_s} \boldsymbol{c}^T\boldsymbol{B}^T r\boldsymbol{D}\boldsymbol{B}\boldsymbol{a} d\Omega \\
&\quad + [2\pi - \beta] \int_{\Omega_v} \boldsymbol{c}^T\boldsymbol{B}^T r\boldsymbol{D}\boldsymbol{B}\boldsymbol{a} d\Omega + 2n \int_{\Omega_v} \boldsymbol{c}^T\boldsymbol{N}^T h_c \boldsymbol{N}\boldsymbol{a} d\Omega + 2\pi \int_{\Gamma_{rc}} \boldsymbol{c}^T\boldsymbol{N}^T r h_c \boldsymbol{N}\boldsymbol{a} d\Gamma \\
&\quad + \beta \int_{\Gamma_{HC}} \boldsymbol{c}^T\boldsymbol{N}^T r h_c \boldsymbol{N}\boldsymbol{a} d\Gamma + [2\pi - \beta] \int_{\Gamma_{vc}} \boldsymbol{c}^T\boldsymbol{N}^T r h_c \boldsymbol{N}\boldsymbol{a} d\Gamma \\
&\quad + [2\pi - \beta] \int_{\Gamma_{vc}} \boldsymbol{c}^T\boldsymbol{N}^T r h_r(\boldsymbol{x}, t) d\Gamma + 2\pi \int_{\Gamma_{rc} \cup \Gamma_b} \boldsymbol{c}^T\boldsymbol{N}^T r h_r(\boldsymbol{x}, t) d\Gamma \\
&\quad = 2n \int_{\Omega_v} \boldsymbol{c}^T\boldsymbol{N}^T h_c T_\infty d\Omega + 2\pi \int_{\Gamma_{rc}} \boldsymbol{c}^T\boldsymbol{N}^T r h_c T_\infty d\Gamma - \theta \int_{\Gamma_b} \boldsymbol{c}^T\boldsymbol{N}^T r \widehat{h} d\Gamma \\
&\quad + \beta \int_{\Gamma_{HC}} \boldsymbol{c}^T\boldsymbol{N}^T r h_c T_\infty d\Gamma + [2\pi - \beta] \int_{\Gamma_{vc}} \boldsymbol{c}^T\boldsymbol{N}^T r h_c T_\infty d\Gamma
\end{aligned} \tag{34}$$

After rearranging the eq. 34 to break out the arbitrary coefficient **c**, it is noted that the equation inside the bracket is the zero vector. Which means the arbitrary coefficient **c** can be ignored. With further rearranging to break out $\dot{a}$ and a the equation arrives at the semi-discrete FE-form that can be written as:

$$\left[2\pi \int_{\Omega_s} \boldsymbol{N}^T r\rho_d c_d \boldsymbol{N} d\Omega + [2\pi-\beta] \int_{\Omega_v} \boldsymbol{N}^T r\rho_d c_d \boldsymbol{N} d\Omega\right]\dot{\boldsymbol{a}}$$
$$+\left[2\pi \int_{\Omega_s} \boldsymbol{B}^T r\boldsymbol{D}\boldsymbol{B} d\Omega + [2\pi-\beta] \int_{\Omega_v} [\boldsymbol{B}^T r\boldsymbol{D}\boldsymbol{B}\boldsymbol{a} + 2n\boldsymbol{N}^T h_c \boldsymbol{N}] d\Omega + 2\pi \int_{\Gamma_{rc}} \boldsymbol{N}^T r h_c \boldsymbol{N} d\Gamma\right.$$
$$\left.+\beta \int_{\Gamma_{HC}} \boldsymbol{N}^T r h_c \boldsymbol{N} d\Gamma + [2\pi-\beta] \int_{\Gamma_{vc}} \boldsymbol{N}^T r h_c \boldsymbol{N} d\Gamma\right]\boldsymbol{a} + [2\pi-\beta] \int_{\Gamma_{vc}} \boldsymbol{N}^T r h_r(\boldsymbol{x},t) d\Gamma$$
$$+2\pi \int_{\Gamma_{rc}\cup\Gamma_b} \boldsymbol{N}^T r h_r(\boldsymbol{x},t) d\Gamma$$
$$= 2n \int_{\Omega_v} \boldsymbol{N}^T h_c T_\infty d\Omega + 2\pi \int_{\Gamma_{rc}} \boldsymbol{N}^T r h_c T_\infty d\Gamma - \theta \int_{\Gamma_b} \boldsymbol{N}^T r q_b d\Gamma + \beta \int_{\Gamma_{HC}} \boldsymbol{N}^T r h_c T_\infty d\Gamma$$
$$+[2\pi-\beta] \int_{\Gamma_{vc}} \boldsymbol{N}^T r h_c T_\infty d\Gamma \quad (35)$$

3.2.5 Time discretization

For the system to be solved algorithmically, the semi-discrete FE-form needs to be a fully discrete system of equations. Which is done by performing a time discretization of the semi-discrete FE-form done in section 3.2.4, and by linearizing the radiation and after that discretize it.
The time discretization is done by splitting the continuous time domain into intervals between the time nodes,
$t_0 < t_1 < t_2 < \cdots < t_{total}$. The temperature of each time step, $\boldsymbol{a}(t)$, is approximated as:

$$\boldsymbol{a}(t) \approx [1-\alpha]\boldsymbol{a}_n + \alpha \boldsymbol{a}_{n+1}, \qquad \alpha \in [0,1], \qquad t \in [t_n, t_{n+1}] \quad (36)$$

and its time derivative as:

$$\dot{\boldsymbol{a}} = \frac{\boldsymbol{a}_{n+1} - \boldsymbol{a}_n}{\Delta t}, \qquad \Delta t = t_{n+1} - t_n \quad (37)$$

For the system to be fully discrete the radiation term must also be discretized, which has been left for now because of its nonlinearity. The energy loss from radiation is obtained from Boltzmann law of radiation,

$$h_r(T) = \varepsilon_e \sigma [T^4 - T_\infty^4] \quad (2)$$

where ε_e is the emissivity, σ is the Steffan Boltzmann constant, T is the temperature and T_∞ is the ambient temperature.

Since the radiation formula is non-linear it must be linearized for the integrals to be discretized into finite elements. This is done by doing a linear approximation of the function using the first order Taylor polynomial expansion of eq. (2).

$$h_r(T) = h_r(T^*) + \frac{\partial h_r(T^*)}{\partial T}[T - T^*] = \varepsilon_e \sigma [T^{*4} - T_\infty^4] + 4\varepsilon_e \sigma T^{*3}[T - T^*] = \varepsilon_e \sigma [-3T^{*4} - T_\infty^4 + 4T^{*3} T] \quad (38)$$

T^* is the temperature in the previous time step and cand also be explained as $T^* = T_{n-1}$. Discretize and insert into the fully discrete FE-form. Replace the term $h_r(\boldsymbol{x}, t)$ in eq. 35 with eq. 38, also replace

the terms $\boldsymbol{a}(t)$ and $\dot{\boldsymbol{a}}$ with eq. 36 and 37 respectively. The fully discrete FE-form can be seen in eq. 39 and to see it fully written out check the appendix.

$$[\boldsymbol{C}^s + \boldsymbol{C}^v]\frac{\boldsymbol{a}_{n+1} - \boldsymbol{a}_n}{\Delta t} + [\boldsymbol{K}^s + \boldsymbol{K}^v + \boldsymbol{K}_c^b + \boldsymbol{K}_c^{rc} + \boldsymbol{K}_c^{HC} + \boldsymbol{K}_c^{VC}]\big[[1-\alpha]\boldsymbol{a}_n + \alpha\boldsymbol{a}_{n+1}\big] = \boldsymbol{f}_c^v + \boldsymbol{f}_b^b + \boldsymbol{f}_b^{rc} + \boldsymbol{f}_b^{HC} + \boldsymbol{f}_b^{VC} \tag{39}$$

Where:

$$\boldsymbol{C}^s = 2\pi\int_{\Omega_s}\boldsymbol{N}^T r\rho_d c_d \boldsymbol{N} d\Omega \qquad \boldsymbol{C}^v = [2\pi-\beta]\int_{\Omega_v}\boldsymbol{N}^T r\rho_d c_d \boldsymbol{N} d\Omega$$

$$\boldsymbol{K}^s = 2\pi\int_{\Omega_s}\boldsymbol{B}^T r\boldsymbol{D}\boldsymbol{B} d\Omega \qquad \boldsymbol{K}^v = [2\pi-\beta]\int_{\Omega_v}\boldsymbol{B}^T r\boldsymbol{D}\boldsymbol{B} d\Omega + 2n\int_{\Omega_v}\boldsymbol{N}^T h_c \boldsymbol{N} d\Omega$$

$$\boldsymbol{K}_c^b = 2\pi\int_{\Gamma_b} 4\boldsymbol{N}^T r\varepsilon_e\sigma T^{*3}\boldsymbol{N} d\Gamma \qquad \boldsymbol{K}_c^{rc} = 2\pi\int_{\Gamma_{rc}}\boldsymbol{N}^T r h_c \boldsymbol{N} d\Gamma$$

$$\boldsymbol{K}_c^{HC} = \beta\int_{\Gamma_{HC}}\boldsymbol{N}^T r h_c \boldsymbol{N} d\Gamma \qquad \boldsymbol{K}_c^{VC} = [2\pi-\beta]\int_{\Gamma_{vc}}\boldsymbol{N}^T r h_c \boldsymbol{N}\boldsymbol{a} d\Gamma + [2\pi-\beta]\int_{\Gamma_{vc}}\boldsymbol{N}^T r h_r(\boldsymbol{x},t) d\Gamma$$

$$\boldsymbol{f}_c^v = 2n\int_{\Omega_v}\boldsymbol{N}^T r h_c T_\infty d\Omega$$

$$\boldsymbol{f}_b^b = \int_{\Gamma_b}\boldsymbol{N}^T[2\pi r\varepsilon_e\sigma[3T^{*4} + T_\infty^4] - \theta r q_b] d\Gamma \qquad \boldsymbol{f}_b^{rc} = 2\pi\int_{\Gamma_{rc}}\boldsymbol{N}^T\big[r h_c T_\infty + r\varepsilon_e\sigma[3T^{*4} + T_\infty^4]\big] d\Gamma$$

$$\boldsymbol{f}_b^{VC} = [2\pi-\beta]\int_{\Gamma_{VC}}\boldsymbol{N}^T\big[r h_c T_\infty + r\varepsilon_e\sigma[3T^{*4} + T_\infty^4]\big] d\Gamma \qquad \boldsymbol{f}_b^{HC} = \beta\int_{\Gamma_{HC}}\boldsymbol{N}^T r h_c T_\infty d\Gamma$$

To make the equations more manageable the stiffness matrices and force matrices were combined into $\widetilde{\boldsymbol{K}}$ and $\widetilde{\boldsymbol{F}}$.

$$\widetilde{\boldsymbol{K}} = \boldsymbol{K}^s + \boldsymbol{K}^v + \boldsymbol{K}_c^b + \boldsymbol{K}_c^{rc} + \boldsymbol{K}_c^{HC} + \boldsymbol{K}_c^{VC} \tag{40}$$

$$\widetilde{\boldsymbol{F}} = \boldsymbol{f}_c^v + \boldsymbol{f}_b^b + \boldsymbol{f}_b^{rc} + \boldsymbol{f}_b^{HC} + \boldsymbol{f}_b^{VC} \tag{41}$$

Since the external heat vector is time dependent it is discretized in the same fashion:

$$\widetilde{\boldsymbol{F}}(t) \approx [1-\alpha]\widetilde{\boldsymbol{F}}_n + \alpha\widetilde{\boldsymbol{F}}_{n+1} \tag{42}$$

Inserting the previously derived equations 40, 41 and 42 into previously derived eq. 39 $\Rightarrow$

$$\big[\widetilde{\boldsymbol{C}} + \alpha\Delta t\widetilde{\boldsymbol{K}}\big]a_{n+1} = \Delta t\Big[[1-\alpha]\widetilde{\boldsymbol{F}}_n + \alpha\widetilde{\boldsymbol{F}}_{n+1} - [1-\alpha]\widetilde{\boldsymbol{K}}a_n\Big] + \boldsymbol{C}\boldsymbol{a}_n \tag{43}$$

Where $\boldsymbol{a}_n$ is the known temperature for every node in the previous time step.

$$\boldsymbol{a}_n - known$$

3.2.6 Linear triangular axisymmetric heat flow element

3.2.5.1 Shape functions

For a triangle element with 3-nodes that have the nodal coordinates x_a and y_a, are given by:

$$N_a^e = L_a = \frac{\Delta_a}{\Delta}, \qquad a = 1,2,3 \tag{44}$$

where Δ is the element triangles area and Δ_a is the area of the triangle element's numerator. The numerator is defined by any point P within the element and a represents the nodes in the element.

$$\Delta = \frac{r_1 b_1 + r_2 b_2 + r_3 b_3}{2}, \qquad a = 1,2,3 \tag{45}$$

$$\Delta_a = \frac{a_a + b_a r + c_a z}{2}, \qquad a = 1,2,3 \tag{46}$$

Where:

$$\begin{array}{lll} a_1 = x_2 y_3 - x_3 y_2 & b_1 = y_2 - y_3 & c_1 = x_3 - x_2 \\ a_2 = x_3 y_1 - x_1 y_3 & b_2 = y_3 - y_1 & c_2 = x_1 - x_3 \\ a_3 = x_1 y_2 - x_2 y_1 & b_3 = y_1 - y_2 & c_3 = x_2 - x_1 \end{array}$$

and (r, z) are the global coordinates of point P.

$$N_1^e + N_2^e + N_3^e = 1$$
$$L_1 + L_2 + L_3 = 1$$

Zienkiewicz et al., 2013)

3.2.5.2 Integration of finite element matrices

Contribution from each element is assembled into global damping and stiffness matrices, as well as the global force vectors.

$$\boldsymbol{C}^s = \bigwedge_{e=1}^{n_{sel}} C^{se} \qquad \boldsymbol{C}^v = \bigwedge_{e=1}^{n_{vel}} C^{ve}$$

$$\boldsymbol{K}^s = \bigwedge_{e=1}^{n_{sel}} \boldsymbol{K}^{se} \qquad \boldsymbol{K}^v = \bigwedge_{e=1}^{n_{vel}} \boldsymbol{K}^{ve}$$

$$\boldsymbol{K}_c^b = \bigwedge_{e=1}^{n_{bel}} \boldsymbol{K}_c^{be} \qquad \boldsymbol{K}_c^{rc} = \bigwedge_{e=1}^{n_{rcel}} \boldsymbol{K}_c^{rce} \qquad \boldsymbol{K}_c^{HC} = \bigwedge_{e=1}^{n_{HCel}} \boldsymbol{K}_c^{HCe} \qquad \boldsymbol{K}_c^{VC} = \bigwedge_{e=1}^{n_{VCel}} \boldsymbol{K}_c^{VCe}$$

$$\boldsymbol{f}_c^v = \bigwedge_{e=1}^{n_{vel}} \boldsymbol{f}_c^{ve}$$

$$\boldsymbol{f}_b^b = \bigwedge_{e=1}^{n_{bel}} \boldsymbol{f}_b^{be} \qquad \boldsymbol{f}_b^{rc} = \bigwedge_{e=1}^{n_{rcel}} \boldsymbol{f}_b^{rce} \qquad \boldsymbol{f}_b^{HC} = \bigwedge_{e=1}^{n_{HCel}} \boldsymbol{f}_b^{HCe} \qquad \boldsymbol{f}_b^{VC} = \bigwedge_{e=1}^{n_{VCel}} \boldsymbol{f}_b^{VCe}$$

Where $\bigwedge$ is the assembly operator and n_{xel} is the number of elements for the given domain or boundary condition, and the contribution from each element is:

$$\boldsymbol{C}^{se} = 2\pi \int_{\Omega_s^e} \boldsymbol{N}^{eT} r \rho_d c_d \boldsymbol{N}^{\boldsymbol{e}} d\Omega \qquad \boldsymbol{C}^{ve} = [2\pi - \beta] \int_{\Omega_v^e} \boldsymbol{N}^{eT} r \rho_d c_d \boldsymbol{N}^{\boldsymbol{e}} d\Omega$$

$$\boldsymbol{K}^{se} = 2\pi \int_{\Omega_s^e} \boldsymbol{B}^{eT} r \boldsymbol{D} \boldsymbol{B}^{\boldsymbol{e}} d\Omega \qquad \boldsymbol{K}^{ve} = [2\pi - \beta] \int_{\Omega_v^e} \boldsymbol{B}^{eT} r \boldsymbol{D} \boldsymbol{B}^{\boldsymbol{e}} d\Omega +$$

$$2n \int_{\Omega_v^e} \boldsymbol{N}^{eT} h_c \boldsymbol{N}^{\boldsymbol{e}} d\Omega$$

$$\boldsymbol{K}_c^{be} = 2\pi \int_{\Gamma_b^e} 4\boldsymbol{N}^{eT} r \varepsilon_e \sigma T^{*3} \boldsymbol{N}^{\boldsymbol{e}} d\Gamma \qquad \boldsymbol{K}_c^{rce} = 2\pi \int_{\Gamma_{rc}^e} \boldsymbol{N}^{eT} [r h_c + 4 r \varepsilon_e \sigma T^{*3}] \boldsymbol{N}^{\boldsymbol{e}} d\Gamma$$

$$\boldsymbol{K}_c^{HCe} = \beta \int_{\Gamma_{HC}^e} \boldsymbol{N}^T r h_c \boldsymbol{N} d\Gamma \qquad \boldsymbol{K}_c^{VCe} = [2\pi - \beta] \int_{\Gamma_{VC}^e} \boldsymbol{N}^T [r h_c + 4 r \varepsilon_e \sigma T^{*3}] \boldsymbol{N} d\Gamma$$

$$\boldsymbol{f}_c^{ve} = 2n \int_{\Omega_v^e} \boldsymbol{N}^{eT} r h_c T_\infty dS$$

$$\boldsymbol{f}_b^b = \frac{1}{2\pi} \int_{\Gamma_b^e} \boldsymbol{N}^{eT} [2\pi r \varepsilon_e \sigma [3T^{*4} + T_\infty^4] - \theta r q_b] d\Gamma \qquad \boldsymbol{f}_b^{rce} = 2\pi \int_{\Gamma_{rc}^e} \boldsymbol{N}^{eT} \left[r h_c T_\infty + r \varepsilon_e \sigma [3T^{*4} + T_\infty^4] \right] d\Gamma$$

$$\boldsymbol{f}_b^{HCe} = \frac{\beta}{2\pi} \int_{\Gamma_{HC}^e} \boldsymbol{N}^{eT} r h_c T_\infty d\Gamma \qquad \boldsymbol{f}_b^{VCe} = [2\pi - \beta] \int_{\Gamma_{VC}^e} \boldsymbol{N}^{eT} \left[r h_c T_\infty + r \varepsilon_e \sigma [3T^{*4} + T_\infty^4] \right] d\Gamma$$

The element nodal shape functions are defined as:

$$\boldsymbol{N}^e = [N_1^e \quad N_2^e \quad N_3^e]$$

The global spatial derivates of N_a^e is determined as:

$$\boldsymbol{B}^e = [B_1^e \quad B_2^e \quad B_3^e]$$

where

$$\boldsymbol{B}_a^e = \frac{1}{2\Delta} \begin{Bmatrix} b_a \\ c_a \end{Bmatrix}, \quad a = 1, 2, 3$$

The equations in the surface integrals are too complicated to be solved mathematically, therefore the numerical integration scheme was used. Therefore, the method for triangular elements in (Zienkiewicz et al., 2013) was followed by using integration points and weights, and the same values were used. The integral is replaced by a sum sampled from a number of integration points, often called Gauss points, with coordinates spread out inside the element. Each integration point is

weighted, where the total weight of the element is 1. The integration points were used to interpolate the elements' temperature, which makes the accuracy of the simulation correspond to the number of integration points.

$$\boldsymbol{K}^{se} \approx \sum_{k=1}^{n_{IP}} 2\pi \boldsymbol{B}^{eT} r(L_{ak}) \boldsymbol{D} \boldsymbol{B}^{\boldsymbol{e}} \Delta W_k\,, \quad a = 1,2,3$$

$$\boldsymbol{K}^{ve} \approx \sum_{k=1}^{n_{IP}} [2\pi - \beta] \boldsymbol{B}^{eT}(L_{ak}) \boldsymbol{D} \boldsymbol{B}^{\boldsymbol{e}} \Delta W_k + \sum_{k=1}^{n_{IP}} 2n \boldsymbol{N}^{eT} h_c \boldsymbol{N}^{\boldsymbol{e}} \Delta W_k\,, \quad a = 1,2,3$$

$$\boldsymbol{f}_c^{ve} = 2n \int_{\Omega_v{}^e} \boldsymbol{N}^{eT} h_c T_\infty dS \approx \sum_{k=1}^{n_{IP}} 2n \boldsymbol{N}^{eT} h_c T_\infty \Delta W_k\,, \quad a = 1,2,3$$

were

$$r(L_{ak}) = L_{1k} r_1 + L_{2k} r_2 + L_{3k} r_3$$

n_{IP} – the number of integration points
W_k – weight factor of integration point k
Δ – element area
L_{ak} – parent area coordinates (L_1, L_2, L_3) of integration point k

No of IP	Parent area coordinates (L_1, L_2, L_3)	Weights
1	$\frac{1}{3}, \frac{1}{3}, \frac{1}{3}$	1
3	$\frac{2}{3}, \frac{1}{6}, \frac{1}{6}$ $\frac{1}{6}, \frac{2}{3}, \frac{1}{6}$ $\frac{1}{6}, \frac{1}{6}, \frac{2}{3}$	$\frac{1}{3}$ $\frac{1}{3}$ $\frac{1}{3}$
4	$\frac{1}{3}, \frac{1}{3}, \frac{1}{3}$ $\frac{3}{5}, \frac{1}{5}, \frac{1}{5}$ $\frac{1}{5}, \frac{3}{5}, \frac{1}{5}$ $\frac{1}{5}, \frac{1}{5}, \frac{3}{5}$	$-\frac{27}{48}$ $\frac{25}{48}$ $\frac{25}{48}$ $\frac{25}{48}$

Figure 22: Integration point coordinates and weights

At the natural boundary, the only nodal element shape functions of element nodes on the boundary are non-zero. Which means that these shape functions can be treated as one dimensional instead of two dimensional. In this case it is between vertices 1-2 that are along the boundary as shown in Figure 23.

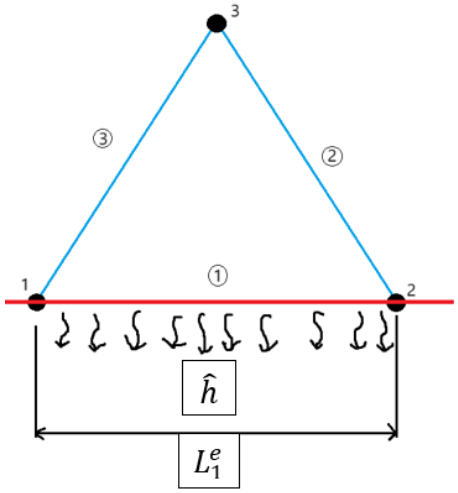

Figure 23: Boundary element with heat outflux

$$f_b^{be}{}_{(3\times1)} = -\int_{\Gamma_{1-2}^e} \theta \begin{Bmatrix} N_1^e \\ N_2^e \\ 0 \end{Bmatrix} r q_b d\Gamma$$

Convert to 1 dimension ⇒

$$f_b^{be}{}_{(2\times1)} = -\int_{\Gamma_{1-2}^e} \theta \begin{Bmatrix} N_1^e \\ N_2^e \end{Bmatrix} r q_b d\Gamma \qquad (47)$$

To compute the shape function as 1D a new coordinate was introduced, which has its origin at vertex 1 and follows the direction along the boundary edge 1-2. Where s is defined as:

$$s = \sqrt{(r - r_1)^2 + (z - z_1)^2} \qquad (48)$$

where (r_1, z_1) are the coordinate of vertex 1. Transform the integration with respect to s by inserting eq. 48 into eq. 47.

$$f_b^{be} = -\int_0^{L_e} \theta \begin{Bmatrix} 1 - \frac{1}{L_e} s \\ \frac{1}{L_e} s \end{Bmatrix} \left[r_1 + \frac{r_2 - r_1}{L_e} s \right] q_b d\Omega = \frac{\theta L_e q_b}{6} \begin{Bmatrix} 2r_1 + r_2 \\ r_1 + 2r_2 \end{Bmatrix} \qquad (49)$$

In the equation L_e is the length of edge 1-2, and is defined as:

$$L_e = \sqrt{(r_r - r_1)^2 + (z_2 - z_1)^2} \qquad (50)$$

Where (r_1, z_1) and (r_2, z_2) are the coordinates for vertex 1 and 2 respectively.

One dimensional numerical Gauss integration was used to compute the element boundary contributions from the convection and radiation boundary integrals. To accomplish this the following steps were used:

1. Start by transforming the boundary integrals to integrals in term of s
2. Transform the integrals to the parent element domain.
   $s = \frac{L_e}{2}\xi + \frac{L_e}{2} \Rightarrow ds = \frac{L_e}{2}d\xi$ where $\xi \in [-1, 1]$
3. Replace the integral with numerical integration with respect to the sum of the integration points and weight factor w_k.

$$\boldsymbol{K}_c^{be} = 2\pi \int_{\Gamma_b^e} 4\boldsymbol{N}^{eT} r\varepsilon_e \sigma T^{*3} \boldsymbol{N}^{\boldsymbol{e}} d\Gamma = 2\pi \int_0^{L_e} 4\boldsymbol{N}^{eT}(s) r(s) \varepsilon_e \sigma T^{*3} \boldsymbol{N}^{\boldsymbol{e}}(s) d\Gamma$$

$$= 2\pi \int_{-1}^{1} 4\boldsymbol{N}^{eT}(\xi) r(\xi) \varepsilon_e \sigma T^{*3} \boldsymbol{N}^{\boldsymbol{e}}(\xi) \frac{L_e}{2} d\xi \approx \sum_{k=1}^{n_{IP}} 8\pi \boldsymbol{N}^{eT}(\xi_k) r(\xi_k) \varepsilon_e \sigma T^{*3} \boldsymbol{N}^{\boldsymbol{e}}(\xi_k) \frac{L_e}{2} w_k$$

$$\boldsymbol{K}_c^{rce} = 2\pi \int_{\Gamma_{rc}^e} \boldsymbol{N}^{eT} [r h_c + 4r\varepsilon_e \sigma T^{*3}] \boldsymbol{N}^{\boldsymbol{e}} d\Gamma = 2\pi \int_0^{L_e} \boldsymbol{N}^{eT}(s) [r(s) h_c + 4r(s)\varepsilon_e \sigma T^{*3}] \boldsymbol{N}^{\boldsymbol{e}}(s) d\Gamma$$

$$= 2\pi \int_{-1}^{1} \boldsymbol{N}^{eT}(\xi) [r(\xi) h_c + 4r(\xi)\varepsilon_e \sigma T^{*3}] \boldsymbol{N}^{\boldsymbol{e}}(\xi) \frac{L_e}{2} d\Gamma$$

$$\approx \sum_{k=1}^{n_{IP}} 2\pi \boldsymbol{N}^{eT}(\xi_k) [r(\xi_k) h_c + 4r(\xi_k)\varepsilon_e \sigma T^{*3}] \boldsymbol{N}^{\boldsymbol{e}}(\xi_k) \frac{L_e}{2} w_k$$

$$\boldsymbol{K}_c^{HCe} = \beta \int_{\Gamma_{HC}^e} \boldsymbol{N}^{eT} r h_c \boldsymbol{N}^e d\Gamma = \beta \int_0^{L_e} \boldsymbol{N}^{eT}(s) r(s) h_c \boldsymbol{N}^e(s) ds = \beta \int_{-1}^{1} \boldsymbol{N}^{eT}(\xi) r(\xi) h_c \boldsymbol{N}^e(\xi) \frac{L_e}{2} d\xi$$

$$\approx \sum_{k=1}^{n_{IP}} \beta \boldsymbol{N}^{eT}(\xi_k) r(\xi_k) h_c \boldsymbol{N}^e(\xi_k) \frac{L_e}{2} w_k$$

$$\boldsymbol{K}_c^{VCe} = [2\pi - \beta] \int_{\Gamma_{VC}^e} \boldsymbol{N}^T [r h_c + 4r\varepsilon_e \sigma T^{*3}] \boldsymbol{N} d\Gamma = [2\pi - \beta] \int_0^{L_e} \boldsymbol{N}^T(s) [r h_c + 4r\varepsilon_e \sigma T^{*3}] \boldsymbol{N}(s) ds$$

$$= [2\pi - \beta] \int_{-1}^{1} \boldsymbol{N}^T(\xi) [r h_c + 4r\varepsilon_e \sigma T^{*3}] \boldsymbol{N}(\xi) \frac{L_e}{2} d\xi$$

$$\approx \sum_{k=1}^{n_{IP}} [2\pi - \beta] \boldsymbol{N}^T(\xi_k) [r h_c + 4r\varepsilon_e \sigma T^{*3}] \boldsymbol{N}(\xi_k) \frac{L_e}{2} w_k$$

$$\boldsymbol{f}_b^{be} = 2\pi \int_{\Gamma_b} \boldsymbol{N}^{eT} r\varepsilon_e \sigma [3T^{*4} + T_\infty^4] d\Gamma = 2\pi \int_0^{L_e} \boldsymbol{N}^{eT}(s) r\varepsilon_e \sigma [3T^{*4} + T_\infty^4] ds$$

$$= 2\pi \int_{-1}^{1} \boldsymbol{N}^{eT}(\xi) r\varepsilon_e \sigma [3T^{*4} + T_\infty^4] \frac{L_e}{2} d\xi \approx \sum_{k=1}^{n_{IP}} 2\pi \boldsymbol{N}^{eT}(\xi_k) r\varepsilon_e \sigma [3T^{*4} + T_\infty^4] \frac{L_e}{2} w_k$$

$$\boldsymbol{f}_b^{rce} = 2\pi \int_{\Gamma_{rc}^e} \boldsymbol{N}^{eT}\left[rh_cT_\infty + r\varepsilon_e\sigma[3T^{*4} + T_\infty^4]\right]d\Gamma = 2\pi \int_0^{L_e} \boldsymbol{N}^{eT}(s)r(s)\left[h_cT_\infty + \varepsilon_e\sigma[3T^{*4} + T_\infty^4]\right]ds$$

$$= 2\pi \int_{-1}^{1} \boldsymbol{N}^{eT}(\xi)r(\xi)\left[h_cT_\infty + \varepsilon_e\sigma[3T^{*4} + T_\infty^4]\right]\frac{L_e}{2}d\xi$$

$$\approx \sum_{k=1}^{n_{IP}} 2\pi\boldsymbol{N}^{eT}(\xi_k)r(\xi_k)\left[h_cT_\infty + \varepsilon_e\sigma[3T^{*4} + T_\infty^4]\right]\frac{L_e}{2}w_k$$

$$\boldsymbol{f}_b^{HCe} = \beta \int_{\Gamma_{HC}^e} \boldsymbol{N}^{eT} rh_cT_\infty d\Gamma = \beta \int_0^{L_e} \boldsymbol{N}^{eT}(s)r(s)h_cT_\infty ds = \beta \int_{-1}^{1} \boldsymbol{N}^{eT}(\xi)r(\xi)h_cT_\infty \frac{L_e}{2}d\xi$$

$$\approx \sum_{k=1}^{n_{IP}} \beta\boldsymbol{N}^{eT}(\xi_k)r(\xi_k)\left[h_cT_\infty + \varepsilon_e\sigma[3T^{*4} + T_\infty^4]\right]\frac{L_e}{2}w_k$$

$$\boldsymbol{f}_b^{VCe} = [2\pi - \beta] \int_{\Gamma_{VC}^e} \boldsymbol{N}^{eT}\left[rh_cT_\infty + r\varepsilon_e\sigma[3T^{*4} + T_\infty^4]\right]d\Gamma$$

$$= [2\pi - \beta] \int_0^{L_e} \boldsymbol{N}^{eT}(s)r(s)\left[h_cT_\infty + \varepsilon_e\sigma[3T^{*4} + T_\infty^4]\right]ds$$

$$= [2\pi - \beta] \int_{-1}^{1} \boldsymbol{N}^{eT}(\xi)r(\xi)\left[h_cT_\infty + \varepsilon_e\sigma[3T^{*4} + T_\infty^4]\right]d\xi$$

$$\approx \sum_{k=1}^{n_{IP}} [2\pi - \beta]\boldsymbol{N}^{eT}(\xi_k)r(\xi_k)\left[h_cT_\infty + \varepsilon_e\sigma[3T^{*4} + T_\infty^4]\right]\frac{L_e}{2}w_k$$

4. Simulation result

4.1 MATLAB Code

An already existing MATLAB code for an axisymmetric transient heat flow model was given by VVC to be modified for the enriched model. In the original model the ventilation layer is simplified to be fully axisymmetric with solid material and with convection on the surrounding edges. The ventilation layer will have lower heat conductivity because of the reduced amount of material, which in the original code is modeled by having a scaling factor for the conduction coefficient, density and specific heat capacity on the ventilation layer. The scaling is obtained by using a calibration tool built into the model and is based on test data from an AMS test.

The code was modified by importing the angles derived in the geometry mapping for each edge and domain and adding them to all the mass, stiffness and force matrices which will be acting as natural scaling. Therefore, the scaling factor was removed. A new force matrix was added for face 5 to include the convection over the vertical surfaces of the vent layer.

4.2 Convergence study

To ensure repeatable and accurate simulations, it is necessary to conduct a convergence study of the model. This verifies that further refinement does not significantly change the result, confirming that the solution has become independent of additional refinement, thereby considered converged.

4.2.1 Mesh

To evaluate the mesh, the relative convergence criterion is used to quantitively assess the mesh refinement on the faces 4,5 and 6 on the model. The criterion evaluates the relative difference between successive mesh results as the mesh is progressively refined, and is defined in eq. 51,

$$\varepsilon > \left\| \frac{R_i - R_{i-1}}{R_i} \right\| \tag{51}$$

In this study, R denotes the nodal temperature 2 mm below the friction surface, where R_i represents the result from the current mesh, R_{i-1} represents the result from the immediately prior mesh and ε is the relative convergence metric. The mesh is considered converged when the relative change decreases below a chosen tolerance, reflecting accepted uncertainty. This behavior is illustrated in Figure 24, which presents the normalized convergence trend observed for the enriched axisymmetric model and computational time.

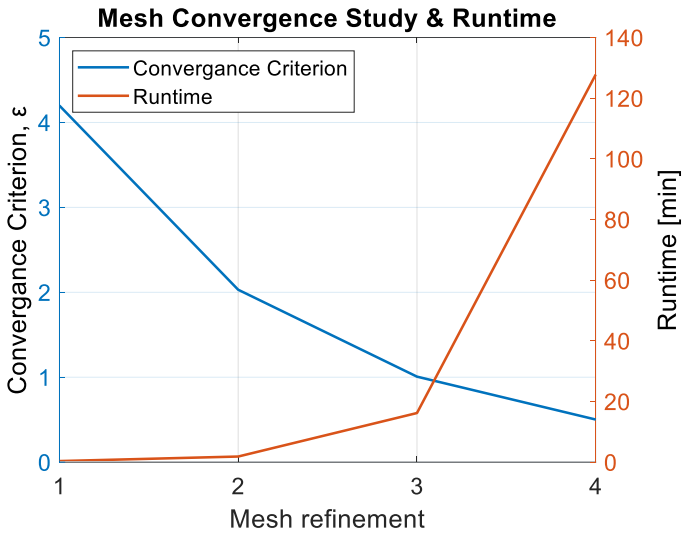

Figure 24: Mesh refinement vs convergence criterion and runtime

The figure shows that temperature converges with mesh refinement, while runtime increases exponentially. Mesh refinement 2 times is deemed appropriate with only 2% relative change in temperature, providing a satisfactory balance between computational cost and solution accuracy, and is adopted for all subsequent simulations. The resulting FE-mesh is depicted in Figure 25, with the element where the temperature is measured highlighted.

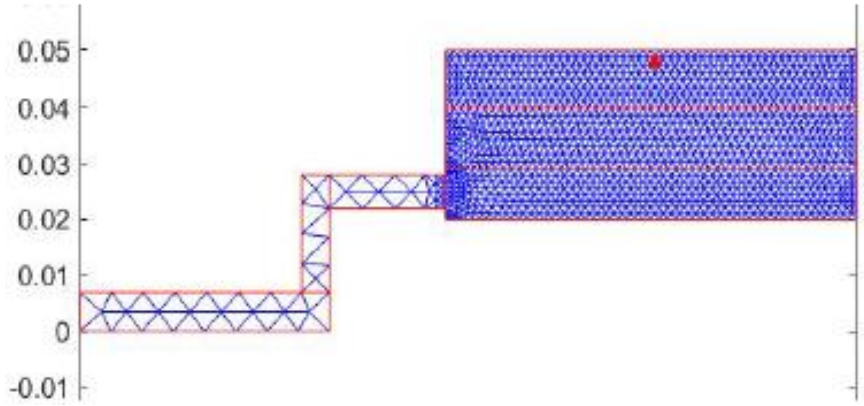

Figure 25: FE mesh. Highlighted is the element where the temperature is measured.

4.3 Transient heat flow 3D model

During the project, VCC developed a 3D transient heat flow model for brake rotors in parallel with the enriched 2D model. The 3D model preserves the full geometric complexity of a VCC brake rotor and functions as a high-fidelity reference to assess the accuracy of the enriched model.

The computational mesh of the 3D model is illustrated in Figure 26, highlighted is the measurement along a circumferential path at the same depth and effective radius as the enriched model.

Temperature along this path is averaged to enable a meaningful comparison with the enriched model, which cannot capture such circumferential temperature variations.

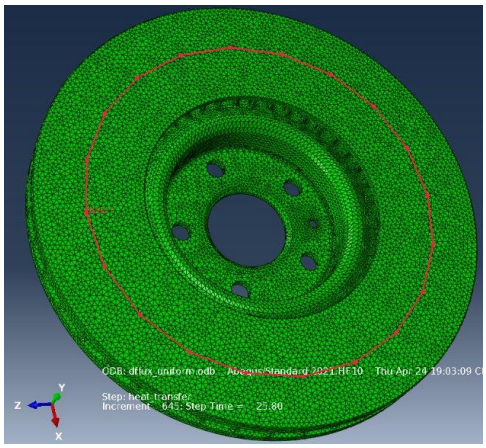

Figure 26: FE mesh 3D reference. Highlighted is the path where the temperature is measured.

By applying the same parameters, boundary conditions, and material properties across the 3D, 2D, and enriched 2D model, it is possible to verify the result against the 3D reference model. Where the 2D model refers to the axisymmetric model supplied by VCC that approximates the vent layer by changing the material properties at this layer and the convection coefficient at this layer. The enriched 2D model refers to the axisymmetric model developed in this thesis where the vent layer is approximated by calculating the amount of surface area and total vane volume. This allows for evaluating each model's thermal behavior, identifying what is accurately captured and limitations in simplified models.

4.4 Verification of enriched 2D model

The results from the enriched 2D model were validated though comparison with the 3D model, considered as reference, and VCC 2D axisymmetric model. To ensure meaningful comparison, all models were configured using the same parameters, including material properties, convection coefficients, geometry, frictional heat input, and radiation coefficients. For the purposes of these tests, the material properties of the brake are simplified to not vary with respect to the temperature.

4.4.1 Simulation with only friction heat

For the first verification the comparison is between the 3D model and the enriched 2D model, with convection and radiation neglected and only friction heat from braking AMS cycle as the thermal input. Temperature is measured at a depth of 2 mm at the effective radius on both models. The friction heat is uniformly distributed on the friction surface over the entire surface area.

The purpose of the test is to ensure that the material proportions remain the same in the conversion from 3D to 2D in respect to the vents. This will affect the heat capacity of the of the model and in turn how much the temperature increases in respect of the energy input.

A time-dependent temperature plot comparing the two models is shown in Figure 27. The result of the enriched 2D model closely aligns with the 3D model, with a peak temperature difference of less than 1%, as seen in Figure 28. The temperature difference is most likely because of the idealized geometry of the enriched 2D model.

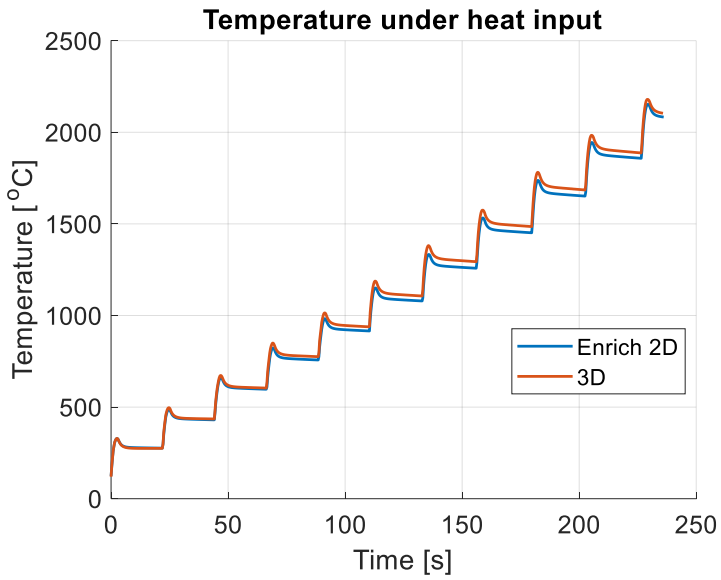

Figure 27: Temperature comparison 2D enriched and 3D model

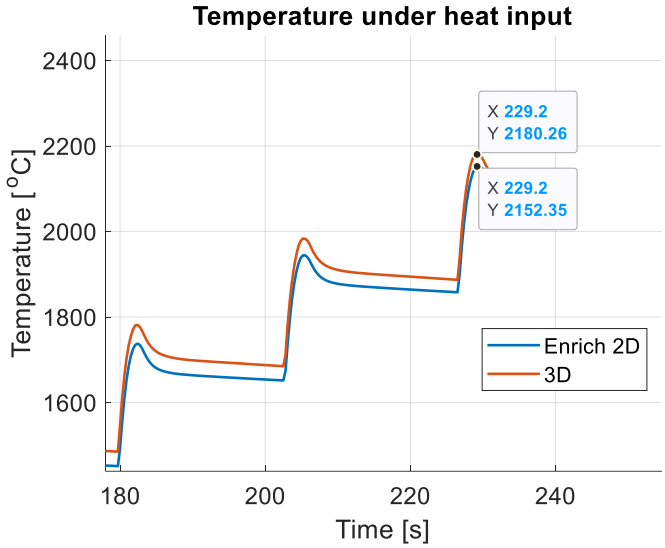

Figure 28: Temperature comparison with peak values

4.4.2 Simulation with friction heat and constant convection

The second comparison is between the enriched 2D model, the 3D model and the VCC 2D axisymmetric model. Frictional heat and convection are uniformly applied, while radiation is neglected. The convection coefficient is constant, without variation due to vehicle speed or position on the brake disc. The models are modeled to have convection on all surfaces of the brake disc, with each surface assigned a convection coefficient of 100 $W/[m^2K]$.

The purpose of this test was to verify that the total surface area of the enriched model corresponds to that of the 3D model. Comparable convective heat loss between the enriched and 3D model would indicate equivalent surfaces areas. This is important since the cooling capabilities of the brake rotor largely depend on its surface area.

Figure 29 illustrates a temperate comparison between the 2D enriched model, the 3D model and VCC 2D axisymmetric model. The results demonstrate that the thermal behavior of the enriched and 3D model follows each other closely, though the deviates is greater than in the setup without convection. In this setup the peak temperatures, as seen in Figure 30, differ by about 5% between the two models. It should be acknowledged that the deviation observed in the heat input in the first

verification also is present here, making the temperature difference not only from disparity in surface area. The form of the temperature curves shows close correspondence, indicating that the modeling of the convection is well captured, although the total surface area is somewhat inflated due to the idealized geometry on this brake rotor.

Furthermore, comparison between the enriched and the VCC 2D model reveals that the enriched model's thermal behavior more closely aligns with the 3D model, as it remains parallel throughout the 11 brake cycles. At cycle 11, the 2D and 3D model exhibit a close temperature agreement. However, this arises from the 2D model underestimating the cooling effect, which causes its temperature to align with that of the 3D model at some point. This implies an improved representation of the cooling effect compared to the VCC 2D model.

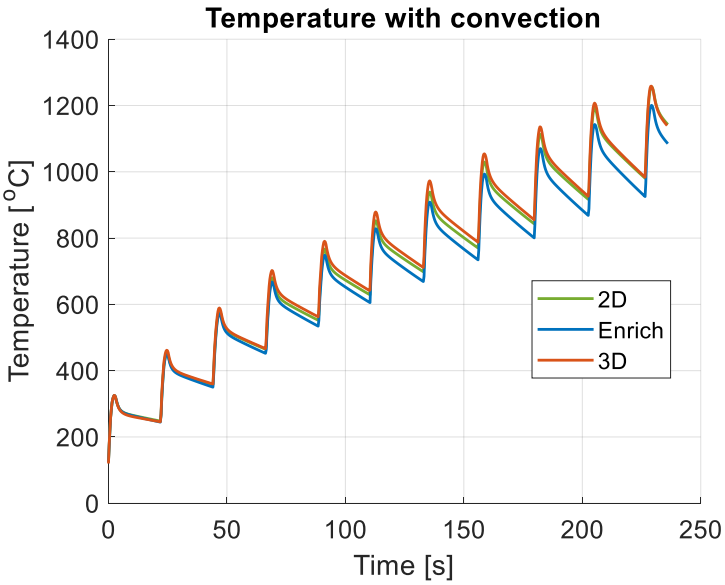

Figure 29: Temperature comparison between 2D, enriched and 3D model with convection

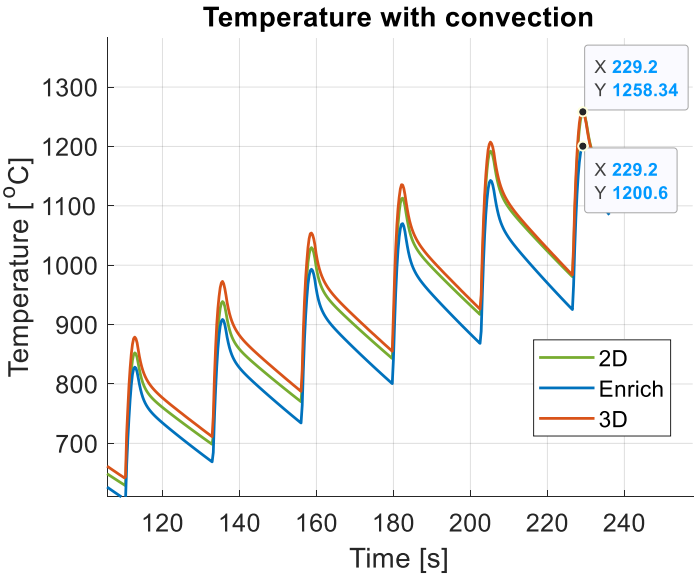

Figure 30: Temperature correlation comparison and peak values between enriched and 3D model

Figure 31 and Figure 32 shows the temperature distribution with convection in the enriched 2D model and the 3D model respectively. A comparison between the two plots shows that the enriched 2D model manages to capture the key features of the 3D model's temperature distribution even with the simplified geometry. In this case it is the lower temperature at the bottom left side of the friction ring caused by conduction out to the hat, which is the part of the brake rotor connected to the wheel hub.

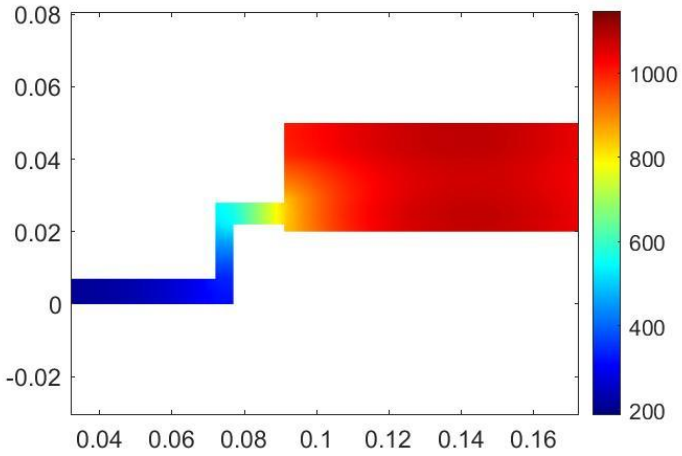

Figure 31: Temperature distribution on enriched 2D model

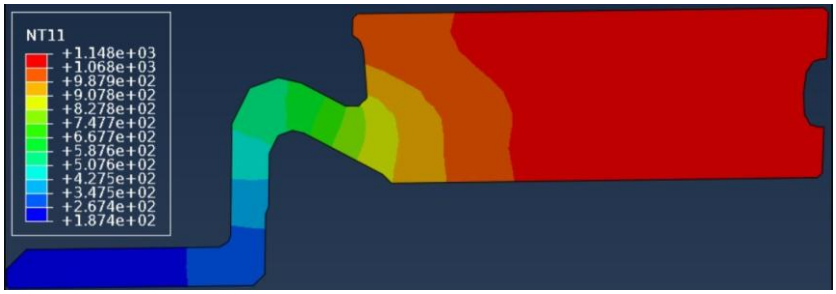

Figure 32: Temperature distribution on 3D model

4.5 Limitation of scaled 2D model

The temperature in the 3D model around a short section of the circumference is plotted in Figure 33 for different depths. In the plot it can be observed that the temperature varies about 10 degrees in the circumferential direction, if the plot is zoomed out it will show that the temperature distribution will change periodically around the entire circumference. The peaks correspond to the position over the ventilated sections; from this it can be inferred that the varied temperature distribution is caused by conduction through the vanes. The scaled 2D model is not able to capture the variation in the temperature distribution around the circumference and will only display the average temperature. The average temperature will also be lower than the peak value on the friction surface.

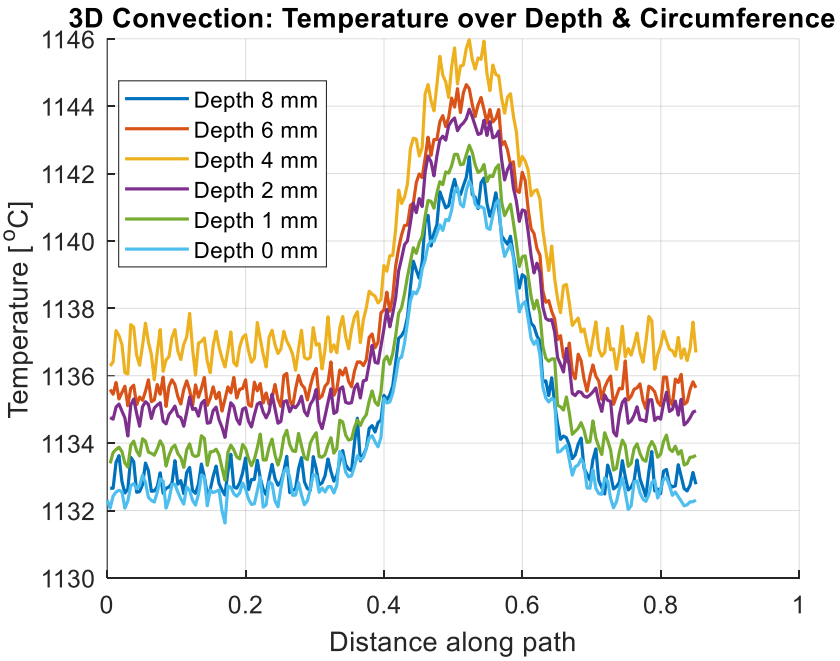

Figure 33: Temperature over depth and circumference

4.6 Temperature over depth

As previously discussed, Figure 33 illustrates temperature variations around the circumference of the 3D model. Averaging these temperature variations at different depths enables a comparison of the thermal behavior of the different models along the depth direction.

Figure 34 presents a scaled and normalized temperature versus depth, with 0 depth corresponding to the friction surface and increasing values approaches the ventilation layer. Temperature is scaled for improved visual representation.

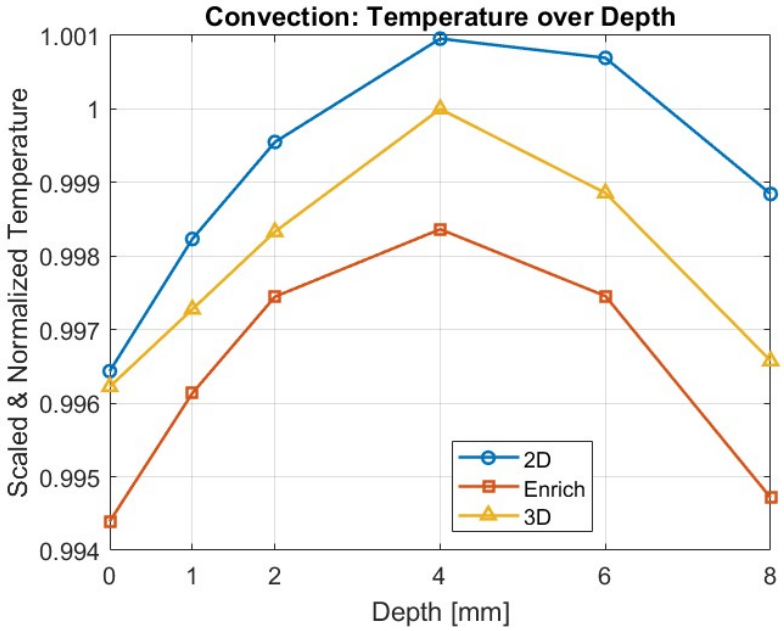

Figure 34: Temperature over depth comparison

From the friction surface to mid-depth of the friction layer, the 2D and Enrich exhibits similar temperature distribution, while the 3D model demonstrates a more linear profile. However, beyond mid-depth toward the ventilation layer, the 2D model deviates, failing to capture the temperature drop observed in the 3D model. In contrast, the enriched model closely replicates the temperature profile of the 3D model, with temperature at both the friction surface and the deepest measuring point showing similar values. These thermal behaviors highlight the enriched model's improved ability to capture the cooling effect of the ventilation layer.

4.7 Processing time comparison

To evaluate computation time, a comparison was conducted between the full 3D finite element model and the enriched 2D model. Both models were set up with equivalent boundary conditions, thermal properties, and comparable mesh densities. Although the simulations were run on different hardware, with the 2D model on a standard laptop and the 3D model on a computing cluster with significant greater computation capacity, which precludes a direct comparison. Nevertheless, the result provides insight into the differences in computation time and usability of each model, with the 2D model requiring 2 min to reach a solution, while the 3D model takes hours.

5. Conclusions

This thesis presents a scaled 2D axisymmetric FE model for predicting heat flow in ventilated rotor brakes, aiming to accurately capturing the ventilation cooling effects while maintaining computational efficiency. The model extends the conventional axisymmetric model by introducing rotational scaling capturing the 3D geometry of the ventilated disc within the 2D domain. This is accomplished by rotationally scaling the pattern axisymmetric surfaces of the 3D model into a homogenized equivalent representation along the boundary edges and ventilation layer face of the scaled model. Similarly, thermal material properties of the ventilation layer such as thermal conductivity, specific heat capacity, and density are homogenized to represent the combined effects of the solid vane material and air passages from the vents. This model specifically targets disc brakes with straight radial vanes, utilizing design inputs such as number of vents, the angle one vent occupies and ventilation thickness. This approach allows ventilation designs changes to scale naturally material properties and boundary condition surfaces without the need for model calibration.

The developed model accurately predicts heat flow comparable to a 3D model with convection and cyclic uniformly distributed heat flux, capturing the geometric complexity of a VCC production ventilated brake disc. The model demonstrates 5% deviation relative to the 3D reference model with convention and uniform heat flux, while preserving computational efficiency of a 2D model. An inherent limitation to the scaled model is that it cannot capture the periodic circumferential temperature distribution caused by each vane, which the 3D model captures. The scaled 2D model can only capture the average temperature of the circumferential direction of the disc, meaning that the modeled peak surface temperature will be a little lower than reality. These results suggest that the proposed model delivers sufficient accuracy comparable to a 3D FE model while serving as a computationally efficient tool for thermal analysis of ventilated disc brakes during the early design stage. However, to confidently apply the model in early-stage brake design, further validation is necessary, including verification of the linearized radiation model and comparison with experimental testing.

6. Future work

The next step in the project would be to compare the result of the 2D axisymmetric model with the measured temperature of an AMS test, using it to validate the model and make possible calibrations. This is required for the model to be fully validated, since comparing it to a real-world example is the only reliable way to ensure that the model works. However, accurate convection and radiation coefficients for each surface of the brake rotor during the AMS test are needed for accurate modeling. This data is not easy to acquire and due to lack of time this must be future work. The model should also be validated against other brake rotors.

Further work would also be to implement changing convection coefficients, based on the position on the brake rotor and the velocity of the vehicle, into the code. As well as the conduction and radiation coefficients changing based on the temperature of the brake rotor. This would require updates in the scaled 2D model's code and further development of the 3D model.

Future work could also involve extending the 2D model in the circumferential direction using reduced order modeling techniques.

References

Bhandari, N., & Mane, P. (2020). *Finite Element Analysis of Thermal Buckling in Automotive Clutch Plate Disc*. https://www.researchgate.net/publication/341371756_Finite_Element_Analysis_of_Thermal_Buckling_in_Automotive_Clutch_Plate_Disc

Brake-tests imc Test & Measurement GmbH. (n.d.). Retrieved June 3, 2025, from https://www.imc-tm.nl/solutions/vehicles/brake-tests

"Centrifugal pumps." (2025). https://www.michael-smith-engineers.co.uk/resources/useful-info/centrifugal-pumps

Charron, F., & Vernotte Pierre. (1939). *Partage de la chaleur entre deux corps frottants - Google Books*. https://www.google.se/books/edition/Partage_de_la_chaleur_entre_deux_corps_f/ZKJPAAAAYAAJ?hl=sv&gbpv=0&bsq=Fernand%20Charron%20and%20Pierre%20Vernotte.%20%E2%80%9CPartage%20de%20la%20chaleur%20entre%20deux%20corps%20frottants%22

COMSOL Multiphysics. (2017). Detailed Explanation of the Finite Element Method (FEM). In *COMSOL Multiphysics* (pp. 1–37). https://www.comsol.com/multiphysics/finite-element-method

Dufré, P. (2005). *Didier Majcherczak Third Body Influence on Thermal Friction Contact Problems: Application to Braking*. https://doi.org/10.1115/1.1757490

F. Talati, & S. Jalalifar. (2008). Investigation of Heat Transfer Phenomena in a Ventilated Disk Brake Rotor with Straight Radial Rounded Vanes. *Applied Sciences*.

G., B., G. E., C., A., P., A., B., & P., P. (2002). *Experimental Investigation of the Mean and Turbulent Flow Characteristics at the Exit of Automotive Vented Brake Discs*. SAE International. https://doi.org/10.4271/2002-01-2590

Lee, S., & Yeo, T. (2000). Temperature and coning analysis of brake rotor using an axisymmetric finite element technique. *Proceedings - KORUS 2000: 4th Korea-Russia International Symposium on Science and Technology*, *3*, 17–22. https://doi.org/10.1109/KORUS.2000.866053

Newcomb, T. P. (1960). *TEMPERATURES REACHED IN DISC BRAKES*.

Sheridan, D. C., Kutchey, J. A., & Samie, F. (1988). Approaches to the Thermal Modeling of Disc Brakes. *SAE Technical Paper 880256*. https://doi.org/https://doi.org/10.4271/880256

Vdovin, A., & Le Gigan, G. (2020). Aerodynamic and thermal modelling of disc brakes - Challenges and limitations. In *Energies* (Vol. 13, Issue 1). MDPI AG. https://doi.org/10.3390/en13010203

Zhang, L., Jia, L., Meng, D., & Liang, J. (2024). A prediction method for convective heat transfer coefficients of brake discs based on small samples combined wind tunnel tests and CFD simulations. *Proceedings of SPIE - The International Society for Optical Engineering*, *13163*. https://doi.org/10.1117/12.3030129

Zienkiewicz, O. C., Taylor, R. L., & Zhu, J. Z. (2013). Shape Functions, Derivatives, and Integration. In *The Finite Element Method: its Basis and Fundamentals*. https://doi.org/10.1016/b978-1-85617-633-0.00006-x

Appendix

A.1 Fully discrete FE-form

$$\left[2\pi \int_{\Omega_s} \boldsymbol{N}^T r\rho_d c_d \boldsymbol{N} d\Omega + [2\pi-\beta] \int_{\Omega_v} \boldsymbol{N}^T r\rho_d c_d \boldsymbol{N} d\Omega\right] \frac{\boldsymbol{a}_{n+1}-\boldsymbol{a}_n}{\Delta t}$$

$$+ \left[2\pi \int_{\Omega_s} \boldsymbol{B}^T r\boldsymbol{D}\boldsymbol{B} d\Omega + [2\pi-\beta] \int_{\Omega_v} \boldsymbol{B}^T r\boldsymbol{D}\boldsymbol{B} d\Omega + 2n \int_{\Omega_v} \boldsymbol{N}^T h_c \boldsymbol{N} d\Omega\right.$$

$$+ 2\pi \int_{\Gamma_b} 4\boldsymbol{N}^T r\varepsilon_e \sigma T^{*3} \boldsymbol{N} d\Gamma + 2\pi \int_{\Gamma_{rc}} \boldsymbol{N}^T [rh_c + 4r\varepsilon_e \sigma T^{*3}] \boldsymbol{N} d\Gamma$$

$$\left. + \beta \int_{\Gamma_{HC}} \boldsymbol{N}^T r h_c \boldsymbol{N} d\Gamma + [2\pi-\beta] \int_{\Gamma_{VC}} \boldsymbol{N}^T [rh_c + 4r\varepsilon_e \sigma T^{*3}] \boldsymbol{N}\boldsymbol{a} d\Gamma\right] [[1-\alpha]\boldsymbol{a}_n$$

$$+ \alpha \boldsymbol{a}_{n+1}]$$

$$= 2n \int_{\Omega_v} \boldsymbol{N}^T h_c T_\infty d\Omega + \int_{\Gamma_b} \boldsymbol{N}^T \left[2\pi r\varepsilon_e \sigma [3T^{*4} + T_\infty^4] - \theta r\hat{h}\right] d\Gamma$$

$$+ 2\pi \int_{\Gamma_{rc}} \boldsymbol{N}^T \left[rh_c T_\infty + r\varepsilon_e \sigma [3T^{*4} + T_\infty^4]\right] d\Gamma$$

$$+ \beta \int_{\Gamma_{HC}} \boldsymbol{N}^T r h_c T_\infty d\Gamma + [2\pi-\beta] \int_{\Gamma_{VC}} \boldsymbol{N}^T \left[rh_c T_\infty + r\varepsilon_e \sigma [3T^{*4} + T_\infty^4]\right] d\Gamma$$